

**SYMMETRY EFFECTS FOR
INELASTIC SCATTERING TO THE
SECOND, UNBOUND, STATE IN
 ${}^9\text{Be}$ ($5/2^-$, 2.43 MeV) IN THE
FERMIONIC SYSTEM ${}^9\text{Be} + {}^9\text{Be}$**

by

Onyinye Ann Umeakubuike

A research report submitted to the Faculty of Science,
University of the Witwatersrand, Johannesburg, in partial fulfillment of the
requirements for the degree of Master of Science.

Johannesburg, 2012

Declaration

I declare that this research report is my own, unaided work. It is being submitted for the partial fulfillment of the requirements for the degree of Masters of Science in the University of the Witwatersrand, Johannesburg. It has not been submitted before for any degree or examination in any other university.

Signature: 

Onyinye Ann Umeakubuike

Date: May 21, 2012

Abstract

Elastic scattering and inelastic excitation of the second, unbound, state ${}^9\text{Be}$ ($5/2^-$, 2.43 MeV) for the identical-particle fermionic system ${}^9\text{Be} + {}^9\text{Be}$ have been measured at the highest incident beam energy presently available $E_{\text{Lab}}({}^9\text{Be}) = 25$ MeV. A ${}^9\text{Be}$ beam, produced by the General Ionex Corporation model 860C sputter ion-source, was accelerated by the EN Tandem Van de Graaff accelerator of the iThemba LABS (Gauteng) and was used to bombard a thin ${}^9\text{Be}$ target. The experimental equipment associated with the C-line includes a high resolution ΔE - E gas-ionisation detector coupled to a small scattering chamber. Energy loss and residual energy signals were processed using a CAMAC-based plus OS/2 WIMPS2 data acquisition system running on an online computer. The ΔE - E plots were used to identify the reaction products and their kinematic energies, thereby determining the elastic and inelastic scattering cross-sections. The elastic and inelastic scattering data were analysed in terms of the optical model and Distorted Wave Born Approximation, respectively. Angular distribution data for the elastic scattering for ${}^9\text{Be} + {}^9\text{Be}$ conformed well to the optical model predictions using an energy-independent optical model potential. Inelastic scattering cross-sections were determined up to $\theta_{\text{c.m.}} \approx 135^\circ$ and symmetry effects were investigated. As such, excitation of the second, unbound, state ${}^9\text{Be}$ ($5/2^-$, 2.43 MeV) via a strong $E2$ one-step two-body interaction from the ${}^9\text{Be}$ ($3/2^-$, g.s.) did not show effects due to symmetry in the entrance channel. These results were consistent with a previous study at $E_{\text{Lab}}({}^9\text{Be}) = 16$ MeV.

Dedication

To my beloved husband, Benjamin Okoli.

Acknowledgements

I especially thank my supervisor, Prof. J. M. Carter for his supervision, advice and valuable suggestions during the progress of this research work. His knowledge, enthusiasm and undying energy in research had inspired me. He was always reachable and willing to help, this made my study very smooth and fulfilling.

I greatly thank my co-supervisor Prof. E. Sideras-Haddad for his assistance and crucial contribution. His involvement made this study a success.

I acknowledge iThemba LABS (Gauteng) and the University of the Witwatersrand for their financial support.

I say a big thank you to iThemba LABS (Gauteng) accelerator staff, Mr Oleg Pekar, Mr Gerard Badenhorst and Mr Fritz Balzun, for their assistance in running the EN Tandem accelerator. The general support from iThemba LABS (Gauteng) staff Ms D. Mahlare and Ms D. Monyamane is greatly appreciated.

I am grateful to Dr Iyabo Usman for offering her advice and suggestions whenever I need them. Many thanks also to my friends and colleagues especially Maxwell and Oscar for their help and best suggestions.

My deepest gratitude goes to my husband, Benjamin Okoli for his unflagging love, prayers, support and encouragement throughout my study.

Last not least, thanks to Almighty God who made everything possible. *Otiti diri Chineke n'elu kacha elu!!*

Table of Contents

Declaration	i
Abstract	ii
Dedication	iii
Acknowledgements	iv
List of Figures	vii
List of Tables.....	ix
CHAPTER 1	
Introduction	1
CHAPTER 2	
Theoretical description	4
2.1 Coulomb scattering.....	4
2.1.1 Rutherford scattering.....	4
2.1.2 Mott scattering of two identical particles.....	7
2.2 Optical model of elastic scattering	9
2.3 Identical-particle symmetric and antisymmetric states	13
2.4 Distorted Wave Born Approximation (DWBA) for inelastic scattering	14
2.4.1 Symmetry effects in inelastic excitation cross-sections.....	16
CHAPTER 3	
Experimental details	17
3.1 Experimental procedures	17
3.1.1 ^9Be beams.....	17
3.1.2 ^9Be target.....	17
3.2 Experimental set-up.....	18
3.2.1 Scattering chamber.....	18

3.2.2	ΔE - E gas-ionisation detector.....	20
3.2.3	Gas delivery system	22
3.2.4	Electronics.....	23
3.3	Data collection and extraction	25
3.4	Evaluation of scattering cross-sections	29
CHAPTER 4		
	Analysis and discussion	32
4.1	Review of ${}^9\text{Be} + {}^9\text{Be}$ scattering and rationale for data collection	32
4.2	Identical particle scattering and intrinsic spin.....	38
4.3	Elastic and inelastic scattering of ${}^9\text{Be} + {}^9\text{Be}$ at $E_{\text{Lab}}({}^9\text{Be}) = 25 \text{ MeV}$	41
4.3.1	Review of the measured data	41
4.3.2	Optical model analysis of elastic scattering.....	42
4.3.3	Distorted Wave Born Approximation (DWBA) analysis of inelastic scattering.....	43
4.4	Discussion	45
CHAPTER 5		
	Conclusions	51
	References	53
	Appendix	55

List of Figures

Figure 2.1: Particle trajectory in Rutherford scattering	5
Figure 2.2: Indistinguishable processes in the scattering of two identical particles	8
Figure 3.1: Experimental equipment associated with the C-line of the 6 MV EN Tandem accelerator at iThemba LABS (Gauteng)	19
Figure 3.2: Schematic drawing of the ΔE - E gas-ionisation detector	21
Figure 3.3: Photograph of the gas delivery system and beam line components ..	23
Figure 3.4: Block diagram of the electronics data acquisition system used in the ${}^9\text{Be} + {}^9\text{Be}$ measurements	24
Figure 3.5: Two dimensional ΔE - E_{total} spectrum for ${}^9\text{Be} + {}^9\text{Be}$ at $E_{\text{Lab}}({}^9\text{Be}) = 25$ MeV and $\theta_{\text{Lab}} = 30^\circ$	26
Figure 3.6: Transformed and projected one dimensional ΔE - E_{total} spectrum of ${}^9\text{Be} + {}^9\text{Be}$ at $E_{\text{Lab}}({}^9\text{Be}) = 25$ MeV and $\theta_{\text{Lab}} = 30^\circ$	27
Figure 3.7: One dimensional monitor detector spectrum for ${}^9\text{Be} + {}^9\text{Be}$ at $E_{\text{Lab}}({}^9\text{Be}) = 25$ MeV and $\theta_{\text{Lab}} = 45^\circ$	30
Figure 4.1: <i>Upper part:</i> Excitation functions for the elastic scattering of ${}^9\text{Be} + {}^9\text{Be}$ at $\theta_{\text{c.m.}} = 90^\circ$ for $E_{\text{Lab}}({}^9\text{Be}) = 3$ to 24 MeV. <i>Lower part:</i> Excitation functions for the elastic scattering of ${}^9\text{Be} + {}^9\text{Be}$ at $\theta_{\text{c.m.}} \approx 50^\circ$ for $E_{\text{Lab}}({}^9\text{Be}) = 6$ to 25 MeV	33
Figure 4.2: Angular distributions for the elastic scattering of ${}^9\text{Be} + {}^9\text{Be}$ at $E_{\text{Lab}}({}^9\text{Be}) = 5$ MeV, 9 MeV, 12 MeV and 16 MeV	34

Figure 4.3: <i>Upper part:</i> Angular distributions for the elastic scattering of ${}^9\text{Be} + {}^9\text{Be}$ at $E_{\text{Lab}} = 16$ MeV. <i>Lower part:</i> Inelastic excitation of the second, unbound, state in ${}^9\text{Be}$ ($5/2^-$, 2.43 MeV) at $E_{\text{Lab}} = 16$ MeV.....	36
Figure 4.4: Inelastic excitation of the second, unbound, state ${}^9\text{Be}$ ($5/2^-$, 2.43 MeV) at $E_{\text{Lab}}({}^9\text{Be}) = 16$ MeV, 25 MeV and 29 MeV	37
Figure 4.5: Energy levels of ${}^9\text{Be}$	39
Figure 4.6: Angular distributions for ${}^9\text{Be} + {}^9\text{Be}$ Coulomb scattering at $E_{\text{Lab}}({}^9\text{Be}) = 25$ MeV, assuming different intrinsic spin values I	40
Figure 4.7: <i>Upper part:</i> Angular distributions for the elastic scattering of ${}^9\text{Be} + {}^9\text{Be}$ at $E_{\text{Lab}}({}^9\text{Be}) = 25$ MeV. <i>Lower part:</i> Inelastic excitation of the second, unbound, state in ${}^9\text{Be}$ ($5/2^-$, 2.43 MeV) at $E_{\text{Lab}}({}^9\text{Be}) = 25$ MeV	47
Figure 4.8: <i>Upper part:</i> Angular distributions for the elastic scattering of ${}^9\text{Be} + {}^9\text{Be}$ at $E_{\text{Lab}}({}^9\text{Be}) = 25$ MeV. <i>Lower part:</i> Inelastic excitation of the second, unbound, state in ${}^9\text{Be}$ ($5/2^-$, 2.43 MeV) at $E_{\text{Lab}}({}^9\text{Be}) = 25$ MeV, showing Coulomb and nuclear excitations.....	48
Figure 4.9: <i>Upper part:</i> Angular distributions for the elastic scattering of ${}^9\text{Be} + {}^9\text{Be}$ at $E_{\text{Lab}}({}^9\text{Be}) = 25$ MeV. <i>Lower part:</i> Inelastic excitation of the second, unbound, state in ${}^9\text{Be}$ ($5/2^-$, 2.43 MeV) at $E_{\text{Lab}}({}^9\text{Be}) = 25$ MeV using incoherent addition.	49
Figure 4.10: <i>Upper part:</i> Angular distributions for the elastic scattering of ${}^9\text{Be} + {}^9\text{Be}$ at $E_{\text{Lab}}({}^9\text{Be}) = 25$ MeV. <i>Lower part:</i> Inelastic excitation of the second, unbound, state in ${}^9\text{Be}$ ($5/2^-$, 2.43 MeV) at $E_{\text{Lab}}({}^9\text{Be}) = 25$ MeV, using coherent addition.....	50

List of Tables

Table 3.1 Bias voltages used for the ΔE - E gas-ionisation detector.....	22
Table 4.1 Inelastic scattering cut-off angle with an entrance window for the ΔE - E gas-ionisation detector system of 1 μm and 0.5 μm thick mylar and 1 kPa isobutane differential pressure for various incident ${}^9\text{Be}$ beam energies.....	38
Table 4.2 Summary of the measured data for ${}^9\text{Be} + {}^9\text{Be}$ scattering at $E_{\text{Lab}}({}^9\text{Be}) = 25$ MeV taken in steps of $\Delta\theta_{\text{Lab}} = 2.5^\circ$	42
Table 4.3 The optical model parameters for ${}^9\text{Be} + {}^9\text{Be}$ [MA11]	43
Table 4.4 Deformation parameters for inelastic scattering from ${}^9\text{Be}$ ($3/2^-$, g.s) to the second, unbound, state ${}^9\text{Be}$ ($5/2^-$, 2.43 MeV).....	44
Table A1: Elastic scattering measured data of ${}^9\text{Be} + {}^9\text{Be}$ at $E_{\text{Lab}}({}^9\text{Be}) = 25$ MeV.	56
Table A2: Inelastic scattering measured data of ${}^9\text{Be} + {}^9\text{Be}$ at $E_{\text{Lab}}({}^9\text{Be}) = 25$ MeV for the second, unbound, state ${}^9\text{Be}$ ($5/2^-$, 2.43 MeV).	57

CHAPTER 1

Introduction

The study of nuclear reactions provides an insight into the nuclear structure and the mechanisms of nuclear processes. Nearly everything known about nuclei has been discovered in scattering experiments. The comparison of scattering experimental data with nuclear model calculations yields details of the structure of individual nuclei.

The nucleus ${}^9\text{Be}$ is known to be a loosely-bound neutron and alpha-particle system [LA88] which breaks up easily into $n + 2\alpha$. The low lying 2.43 MeV $5/2^-$ unbound state of ${}^9\text{Be}$ is strongly excited via a $\Delta L = 2 \hbar$ ($E2$) inelastic scattering process from the $3/2^-$ ground state, unlike other excited states which are only weakly excited. The aim of the present study is to further investigate the interaction of the fermionic ${}^9\text{Be} + {}^9\text{Be}$ system, to extend the already existing ${}^9\text{Be} + {}^9\text{Be}$ scattering data, and to determine the structure and effects due to symmetry of the inelastic excitation of the $5/2^-$ unbound state of ${}^9\text{Be}$. This work follows on from previously measured ${}^9\text{Be} + {}^9\text{Be}$ scattering data [MA11] taken at the EN Tandem accelerator of iThemba LABS (Gauteng). For identical particle scattering symmetry exists about $\theta_{\text{c.m.}} = 90^\circ$, which is dependent on the nature of the system i.e. bosonic (integer spin) or fermionic (half-integer spin).

In the present study, angular distribution for the elastic scattering and inelastic excitation to the second, unbound, state in ${}^9\text{Be}$ ($5/2^-$, 2.43 MeV) in the fermionic system ${}^9\text{Be} + {}^9\text{Be}$ were measured at $E_{\text{Lab}}({}^9\text{Be}) = 25$ MeV. As a starting point, in the recent previous investigation of Mayida [MA11] similar measurements were obtained at $E_{\text{Lab}}({}^9\text{Be}) = 16$ MeV in order to extend the limited existing data of York and Carpenter [YO77]. In addition, the elastic-scattering excitation function data allowed an energy-independent optical model potential to be determined in

the range $3 \text{ MeV} \leq E_{\text{Lab}}(^9\text{Be}) \leq 25 \text{ MeV}$ spanning the region from the Coulomb barrier ($E_{\text{Lab}}^{\text{CB}}(^9\text{Be} + ^9\text{Be}) = 8 \text{ MeV}$) to well above. The measured elastic-scattering angular distributions displayed the expected symmetry about $\theta_{\text{c.m.}} = 90^\circ$ for an identical-particle scattering system. However, angular distribution inelastic-scattering data for ^9Be excitation to its second, unbound, state (via a relatively strong two-body $E2$ excitation process) was limited to a scattering angle just beyond $\theta_{\text{c.m.}} = 90^\circ$. This was due to the relatively low incident beam energy of $E_{\text{Lab}}(^9\text{Be}) = 16 \text{ MeV}$, resulting in the inelastically scattered ^9Be being below the cut-off energy of the ΔE - E gas-ionisation detector system. As such, it is necessary to increase the beam energy in order to investigate possible symmetry effects in the inelastic scattering channel. The maximum beam energy available at the EN Tandem accelerator (highest terminal voltage of 6 MV) using the $^9\text{Be}^{4+}$ charge state is $E_{\text{Lab}}(^9\text{Be}) = 29 \text{ MeV}$. The full energy of 30 MeV is not possible from a 6 MV terminal voltage since the negative ion $^9\text{BeH}^-$ is injected into the accelerator from the ion source (electron attachment to produce $^9\text{Be}^-$ is very weak [MI90]). However, for the present measurements ^9Be beams could only be produced up to $E_{\text{Lab}}(^9\text{Be}) = 25 \text{ MeV}$. As such, kinematic and energy loss calculations indicated that the inelastic scattering angular distribution could be extended well beyond $\theta_{\text{c.m.}} = 90^\circ$ up to close to $\theta_{\text{c.m.}} \approx 130^\circ$ in order to investigate possible symmetry effects. This would be made possible by careful optimization of the high resolution ΔE - E gas-ionisation detector system and the associated electronics.

Measurements of the inelastic scattering cross-section is made possible by detecting the inelastically scattered ^9Be after exciting ^9Be in a two-body process following which it decays into a neutron and two alpha-particles. Symmetry effects may need to be taken into account because of the identical particle entrance channel.

This Research Report is arranged as follows:

- The theoretical description and the models used to analyse the data are outlined in Chapter 2.

- The experimental details of the present study, together with the data collection and extraction procedures are detailed in Chapter 3.
- The analysis and discussion of the present elastic and inelastic scattering data, including a review of the previously measured data are presented in Chapter 4.
- Conclusions and suggestions are given in Chapter 5.
- The tabulated measured elastic and inelastic scattering results can be found in the Appendix at the back of the Research Report.

CHAPTER 2

Theoretical description

Important information on the structure of nuclei and their interactions can be determined through the study of nuclear reactions [JE90]. Nuclear reactions which occur when two nuclear particles collide are described by the projectile, the reaction products, the scattering angle, the amount of energy Q required or released in the reaction, the excitation energy and the spins involved. To study typical nuclear reactions we require a beam, a target and a system for detection [KR88]. Scattering theories are used for the study and analysis of nuclear scattering and reactions [JA70]. In this chapter, theoretical considerations concerning elastic and inelastic-scattering angular distribution analysis using the Optical Model and the Distorted Wave Born Approximation (DWBA), respectively, are presented.

2.1 Coulomb scattering

Coulomb scattering is the scattering of two charged particles, in this case nuclei, off one another as a result of the electrostatic force between them. It can be elastic scattering where the reaction products remain in their ground states without loss of energy to other processes or alternatively inelastic scattering resulting from the exchange of a virtual photon leaving one or both of the reaction products in an excited state [KR88]. Rutherford scattering describes the Coulomb interaction for non-identical particles while for identical particles the more complicated Mott scattering formula which includes effects due to nuclear spin is used.

2.1.1 Rutherford scattering

Elastic Coulomb scattering is also known as Rutherford scattering [KR88]. This occurs for non-identical nuclear particles [BE64]. Figure 2.1 shows the Rutherford

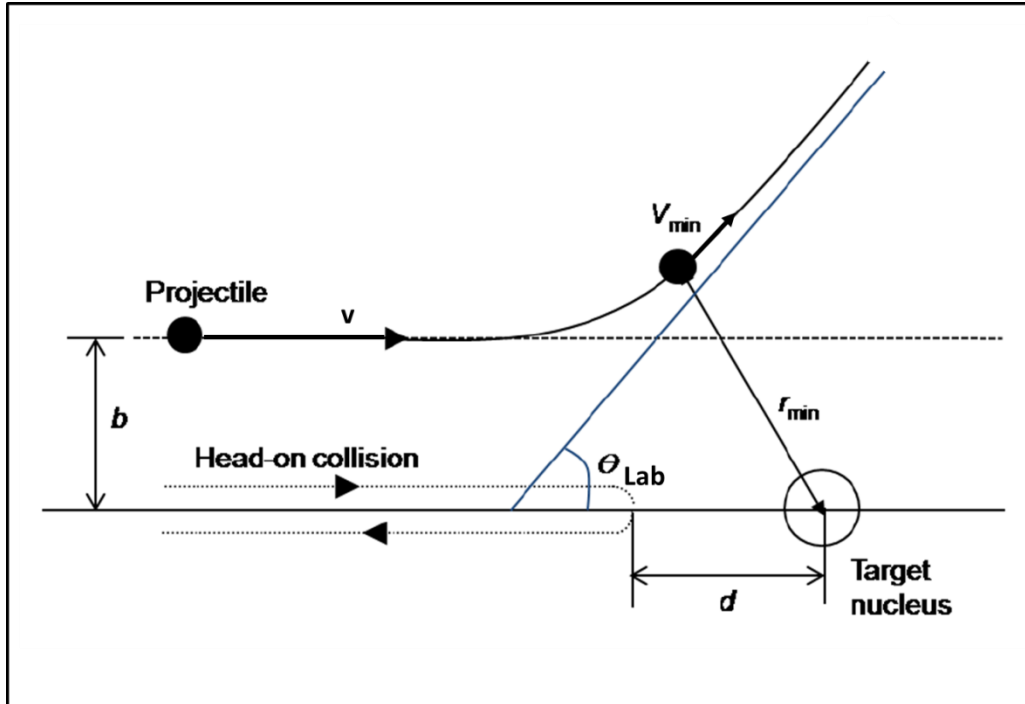


Figure 2.1: Particle trajectory in Rutherford scattering [JI10].

scattering geometry of a particle being scattered by an infinitely-heavy target nucleus.

Because a nucleus contains positively charged protons, the force between two interacting nuclei is repulsive. The long-ranged repulsive Coulomb force is given by

$$F = \frac{Z_1 Z_2 e^2}{4\pi\epsilon_0 r^2}, \quad (2.1)$$

where r is the distance between the projectile and the target nucleus, $Z_1 e$ is the projectile charge and $Z_2 e$ is the target charge. Since the force is repulsive, the trajectory of the scattered particle is hyperbolic. Initially, the projectile approaches the target nucleus with speed v along a line which passes a distance b (impact parameter) between the incident line and the target. The projectile will be

deflected and, therefore, passes the scattering centre through an angle θ_{Lab} (scattering angle).

If b is large, the projectile passes along a path far from the nucleus and the repulsive Coulomb force exerted by the nucleus is weak. The projectile, therefore, has a negligible Coulomb potential energy and its total energy will be the incident kinetic energy. On the other hand, if b is small the projectile passes along a path closer to the target nucleus and experiences a stronger Coulomb force. The Coulomb potential energy of the projectile, therefore, increases to a maximum when reaching a minimum separation distance r_{min} . At r_{min} the projectile moves away from the nucleus and the Coulomb potential energy begins to reduce. If $b = 0$, this results in a head-on collision, where the projectile would recoil in the direction of 180° . At this distance of closest approach, d , the initial kinetic energy is equal to the Coulomb potential energy.

The differential cross-section for Rutherford scattering of non-identical particles is given by [KR88]:

$$\frac{d\sigma}{d\Omega_{\text{c.m.}}} = \left(\frac{Z_1 Z_2 e^2}{4\pi\epsilon_0} \right)^2 \left(\frac{1}{4E_{\text{c.m.}}} \right)^2 \left(\frac{1}{\sin^4 \frac{\theta_{\text{c.m.}}}{2}} \right), \quad (2.2)$$

where

$Z_1 e$ = charge of the projectile,

$Z_2 e$ = charge of the target,

$E_{\text{c.m.}}$ = centre-of-mass energy of the projectile and

$\theta_{\text{c.m.}}$ = centre-of-mass scattering angle.

This is known as the Rutherford's formula for Coulomb scattering. We see from the formula that the magnitude of the Rutherford cross-section depends on Z^2 , $E_{\text{c.m.}}^{-2}$ and $\sin^{-4}(\theta_{\text{c.m.}}/2)$.

2.1.2 Mott scattering of two identical particles

Mott scattering results when two identical particles are involved [BE64]. Quantum mechanically, two identical particles are indistinguishable. In a system of identical bosons (particles with integer spin, including zero) or fermions (particles with half-integer spin), the wave function under the exchange of any two particles must be symmetric or anti-symmetric [SA80], respectively. When a scattering process involves two identical particles, it cannot be distinguished which of the particles emerges from the scattering. As in Fig. 2.2(i), two identical particles A_1 and A_2 undergo scattering, particle A_1 scatters along the direction 1 and A_2 along the direction 2. If the scattering amplitude in the centre-of-mass frame is $f(\theta_{\text{c.m.}})$, the probability $d\sigma/d\Omega_{\text{c.m.}}$ to observe this process is directly proportional to $|f(\theta_{\text{c.m.}})|^2$. In Fig. 2.2(ii), particle A_1 scatters along the direction 2 and A_2 along the direction 1. The probability $d\sigma/d\Omega_{\text{c.m.}}$ to observe this second process is directly proportional to $|f(\pi - \theta_{\text{c.m.}})|^2$, since direction 1 is shifted at an angle $(\pi - \theta_{\text{c.m.}})$. Hence, because A_1 and A_2 are identical, it is impossible to distinguish the two different processes.

The scattering amplitude will then be the sum of the interfering amplitudes for both processes [SA80]:

$$\frac{d\sigma}{d\Omega_{\text{c.m.}}} = |f(\theta_{\text{c.m.}})|^2 \rightarrow |f(\theta_{\text{c.m.}}) + f(\pi - \theta_{\text{c.m.}})|^2. \quad (2.3)$$

The Rutherford scattering formula of Eq. (2.2) then becomes modified for Coulomb scattering of identical point charges and is given by [HO78]:

$$\left. \frac{d\sigma}{d\Omega_{\text{c.m.}}} \right)_I = \frac{\eta^2}{4k^2} \left\{ \csc^4 \frac{\theta_{\text{c.m.}}}{2} + \sec^4 \frac{\theta_{\text{c.m.}}}{2} + \frac{(-)^{2I}}{2I+1} 2\cos\left(\eta \ln \tan^2 \frac{\theta_{\text{c.m.}}}{2}\right) \csc^2 \frac{\theta_{\text{c.m.}}}{2} \sec^2 \frac{\theta_{\text{c.m.}}}{2} \right\}, \quad (2.4)$$

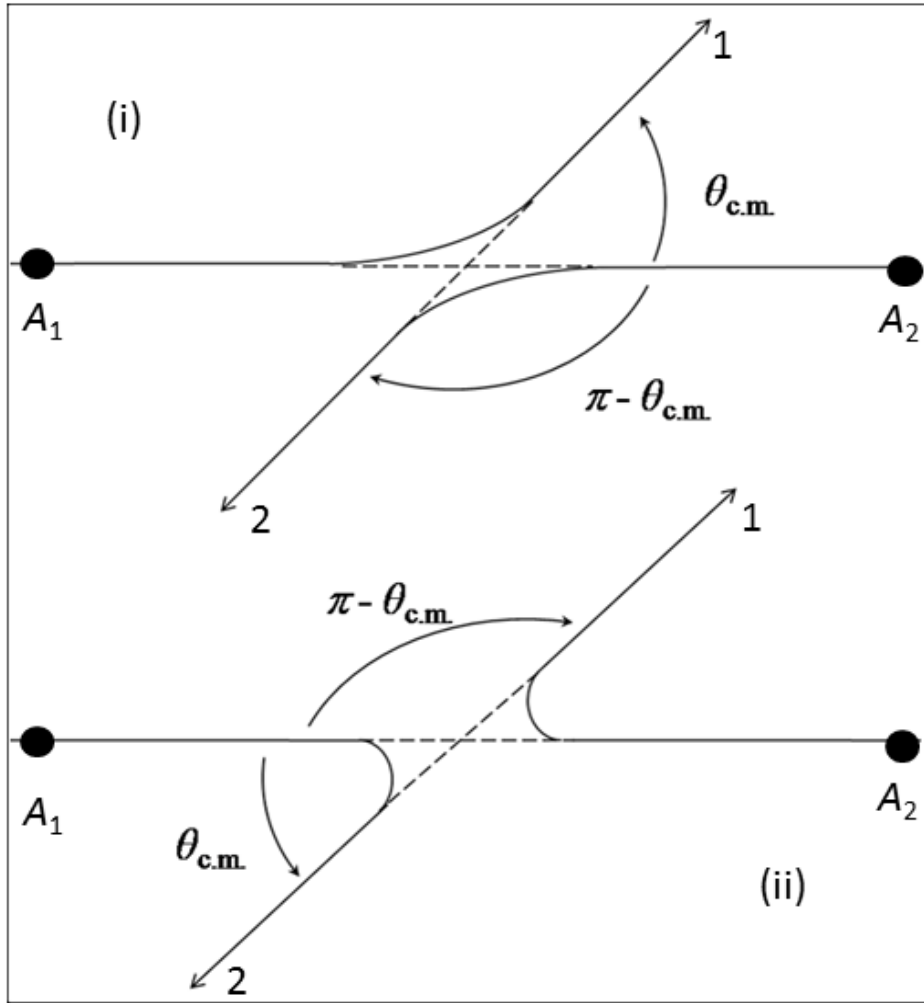


Figure 2.2: Indistinguishable processes in the scattering of two identical particles.

where,

I = total spin of projectile or target,

$\eta = \frac{Z_1 Z_2 e^2 \mu}{\hbar^2 k}$ the dimensionless Sommerfeld parameter and

$k = \left(\frac{2\mu E_{\text{c.m.}}}{\hbar^2} \right)^{1/2}$ the wave number.

This is known as the Mott Scattering formula for identical particles. The third term (interference term) in Eq. (2.4) is responsible for the cross-section's oscillatory structure.

2.2 Optical model of elastic scattering

The optical model of elastic scattering describes the interaction of two nuclei by a complex scattering potential [SA80]. A potential enhances the description of the interaction, by not only describing the strong absorption but also the weak absorption. This model description of nuclei is similar to the scattering and absorption of light by a cloudy crystal ball, hence the name optical model [HO71].

For nuclei of spin zero, the two-body optical-model interaction potential $U(r)$ between the incident and the target nuclei is given by [HO78]:

$$U(r) = U_C(r) + U_N(r), \quad (2.5)$$

where $U_C(r)$ is the Coulomb interaction potential due to a uniform charged distribution of radius $R_C = R_{0C}A_2^{1/3}$, with R_{0C} the Coulomb radius parameter and A_2 the mass of the target. Here, $U_N(r)$ is the nuclear interaction potential and is taken to be complex in order to describe the scattering process which includes absorption of the incident particle flux into non-elastic scattering channels. The nuclear interaction potential is given by

$$U_N(r) = V(r) + iW(r), \quad (2.6)$$

where $V(r)$ and $iW(r)$ are the real and imaginary parts of the scattering potential, respectively. The real part can be energy dependent and takes account of elastic scattering whereas the imaginary part takes account of the loss of incident particle flux from the elastic scattering channel.

A commonly used parametrisation for the scattering potential is the Woods-Saxon form [KR88]. Here, the nuclear interaction potential is written as

$$U_N(r) = V_0 f_R(r) + iW_0 f_I(r), \quad (2.7)$$

where V_0 is the depth of the real potential and W_0 is the depth of the imaginary potential with the volume form representing the geometry of the real and imaginary parts of the potential given by

$$f_{R,I}(r) = \left[1 + \exp\left(\frac{r - R_{R,I}}{a_{R,I}}\right) \right]^{-1}, \quad (2.8)$$

where $R_{R,I} = R_{0R,I} (A_1^{1/3} + A_2^{1/3})$ are the nuclear potential radii and $a_{R,I}$ are the surface diffusenesses.

A derivative of the Wood-Saxon form gives the frequently used surface-absorption imaginary part of the potential [AU78]

$$W(r) = -W_1 \frac{d}{dr} \left[1 + \exp\left(\frac{r - R_1}{a_1}\right) \right]^{-1}, \quad (2.9a)$$

$$W(r) = -W_1 \frac{4 \exp\left(\frac{r - R_1}{a_1}\right)}{\left[1 + \exp\left(\frac{r - R_1}{a_1}\right) \right]^2}. \quad (2.9b)$$

At low incident energies, according to the Pauli Exclusion Principle, only the valence nucleons near the surface can participate in the nuclear reactions, the tightly bound nucleons in the interior cannot. Therefore, Eq. (2.9b) gives an imaginary potential with surface absorption [KR88]. Varying one or more of the six optical model parameters, namely, V_0 , R_{0R} , a_R , W_0 or W_1 , R_{0I} and a_I provides fit to the elastic scattering data.

Considering charged incident particles, the Coulomb potential $U_C(r)$ when r is small ($r \leq R_C$) depends on the assumed uniformly charged sphere of radius $R_C = R_{0C} A_2^{1/3}$, where R_{0C} is the Coulomb radius constant which is obtained from a fit to elastic electron scattering data for the target nucleus. This is given by [BA80]:

$$U_C(r) = \frac{Z_1 Z_2 e^2}{2R_C} \left[3 - \left(\frac{r^2}{R_C^2} \right) \right], \quad r \leq R_C. \quad (2.10a)$$

When r is large ($r > R_C$), the Coulomb potential $U_C(r)$ is given by [BA80]:

$$U_C(r) = \frac{Z_1 Z_2 e^2}{r}, \quad r > R_C. \quad (2.10b)$$

The collision between two charged particles can be described using partial wave theory [JE90]. The partial wave expansion of the wave function when substituted in the Schrödinger equation for a projectile of reduced mass μ and energy E yields the radial wave equation [JA70]:

$$\left[\frac{d^2}{dr^2} + \frac{2\mu}{\hbar^2} (E - U(r)) - \frac{\ell(\ell+1)}{r^2} \right] f_\ell(r) = 0, \quad (2.11)$$

where $f_\ell(r)$ are the radial wave-functions and ℓ the orbital angular momenta. At large values of the separation coordinate r (distance between the centre-of-mass of the projectile to the centre-of-mass of the target), the nuclear field $U(r)$ falls off to zero more rapidly than $1/r$, and so may be neglected. Hence, the radial part of the scattering wave-function can be compared with the Coulomb wave-functions. This comparison gives the phase shifts δ_ℓ .

The scattering amplitude $f(\theta_{\text{c.m.}})$ is related to the differential cross-section for elastic scattering by [BA80]:

$$\frac{d\sigma}{d\Omega_{\text{c.m.}}} = |f(\theta_{\text{c.m.}})|^2. \quad (2.12)$$

Here, $f(\theta_{\text{c.m.}})$ can be expressed in terms of phase shifts δ_ℓ as [HO71]:

$$f(\theta_{\text{c.m.}}) = \frac{1}{2ik} \sum_{\ell=0}^{\infty} (2\ell+1)(S_\ell - 1) P_\ell(\cos\theta_{\text{c.m.}}), \quad (2.13)$$

with

$$S_\ell = \exp(2i\delta_\ell) . \quad (2.14)$$

The complex elastic scattering matrix-elements S_ℓ provide all the information on the interaction [BA80].

The long-range Coulomb interaction affects all partial waves unlike the nuclear interaction which, being short ranged, affects those close to $\ell = 0$. It is, therefore, necessary to split the two effects. Hence, S_ℓ can be defined as

$$S_\ell = \exp[2i(\sigma_\ell + \delta_\ell)] , \quad (2.15)$$

where σ_ℓ and δ_ℓ represent the Coulomb and the nuclear scattering phase shifts, respectively.

The scattering amplitude can then take on the form [JA70]:

$$f(\theta_{\text{c.m.}}) = f_C(\theta_{\text{c.m.}}) + f_N(\theta_{\text{c.m.}}) , \quad (2.16)$$

with the Coulomb scattering amplitude given by

$$\begin{aligned} f_C(\theta_{\text{c.m.}}) &= \frac{1}{2ik} \sum_{\ell=0}^{\infty} (2\ell+1) (e^{2i\sigma_\ell} - 1) P_\ell(\cos \theta_{\text{c.m.}}) \\ &= -\frac{\eta}{2k} \left(\csc \frac{\theta_{\text{c.m.}}}{2} \right)^2 \exp \left[-2\eta \ln \left(\sin \frac{\theta_{\text{c.m.}}}{2} \right) + 2i\sigma_0 \right] , \end{aligned} \quad (2.17)$$

where, σ_ℓ is defined in terms of the gamma function Γ by

$$\sigma_\ell = \arg[\Gamma(\ell+1+i\eta)] . \quad (2.18)$$

Together with nuclear scattering amplitude which is given by

$$f_N(\theta_{\text{c.m.}}) = \frac{1}{2ik} \sum_{\ell=0}^{\infty} (2\ell+1) e^{2i\sigma_\ell} (S_\ell - 1) P_\ell(\cos \theta_{\text{c.m.}}) , \quad (2.19)$$

a final form is obtained

$$f(\theta_{\text{c.m.}}) = f_{\text{C}}(\theta_{\text{c.m.}}) + \frac{1}{2ik} \sum_{\ell=0}^{\infty} (2\ell+1) e^{2i\sigma_{\ell}} (S_{\ell} - 1) P_{\ell}(\cos \theta_{\text{c.m.}}). \quad (2.20)$$

As mentioned previously, all of the information for the scattering process is carried in S_{ℓ} .

2.3 Identical-particle symmetric and antisymmetric states

The total wave-function for all systems of identical particles must be symmetric or antisymmetric under particle exchange: symmetric for bosonic systems and antisymmetric for fermionic systems. In the centre-of-mass system, two identical particles involved in a scattering process cannot be distinguished after elastic scattering has taken place [HO78]. Hence, two states of a system, in which any two identical particles are exchanged, must exchange symmetry. This two particle exchange corresponds to the transformation $\theta_{\text{c.m.}} \rightarrow \pi - \theta_{\text{c.m.}}$. Hence, we can express the scattering amplitude which describes the scattering of the two indistinguishable particles as [BA80]:

$$f_S(\theta_{\text{c.m.}}) = f(\theta_{\text{c.m.}}) + (-1)^S f(\pi - \theta_{\text{c.m.}}), \quad (2.21)$$

where S is the total spin (even for bosons, odd for fermions). The factor $(-1)^S$ gives the scattering amplitude the proper symmetry.

The differential cross-section is always symmetric with respect to $\theta_{\text{c.m.}} = 90^\circ$. For a spin-dependent interaction, the differential cross-section becomes [BA80]:

$$\frac{d\sigma}{d\Omega} = \sum_{S=0}^{2I} \frac{2S+1}{(2I+1)^2} |f_S(\theta_{\text{c.m.}})|^2, \quad (2.22)$$

$$\begin{aligned} &= |f(\theta_{\text{c.m.}})|^2 + |f(\pi - \theta_{\text{c.m.}})|^2 \\ &\quad + \frac{(-1)^{2I}}{2I+1} [f(\theta_{\text{c.m.}}) f^*(\pi - \theta_{\text{c.m.}}) + f^*(\theta_{\text{c.m.}}) f(\pi - \theta_{\text{c.m.}})], \end{aligned} \quad (2.23)$$

where I is the spin quantum number. When the spin I is large, the interference term (third term) becomes very small.

2.4 Distorted Wave Born Approximation (DWBA) for inelastic scattering

The Distorted Wave Born Approximation (DWBA) gives a good description of inelastic scattering to low-lying collective states [TS75]. There is a possibility that kinetic energy will be transferred from the projectile to the target when nuclei collide which can result in inelastic scattering [JE90]. In the first-order DWBA, inelastic scattering is taken to be a one-step transition process. The differential cross-section for inelastic scattering is given by [BA80]:

$$\left. \frac{d\sigma}{d\Omega} \right)_{\text{DWBA}} \propto |T_{fi}|^2. \quad (2.24)$$

In DWBA, the transition amplitude, T_{fi} , describing the inelastic scattering from an initial channel i to a final channel f is given by [JA70]:

$$T_{fi}(k_f, k_i) = \int dr \chi_f^{(-)*}(k_f, r) \langle \Phi_f | U(r, \xi) | \Phi_i \rangle \chi_i^{(+)}(k_i, r), \quad (2.25)$$

where k_i and k_f are the initial and final channel wave-numbers, and $\chi_i^{(+)}(k_i, r)$ and $\chi_f^{(-)*}(k_f, r)$ are the distorted waves that account for the relative motion before and after the inelastic scattering collision. Here, $U(r, \xi)$ is the inelastic scattering interaction potential. This is a function of the internal coordinates ξ of Φ_f (final internal state) and Φ_i (initial internal state).

The interaction potential $U(r, \xi)$ consists of two parts, the Coulomb and the nuclear part, and is given by [JA70]:

$$U(r, \xi) = U_C(r, \xi) + U_N(r, \xi). \quad (2.26)$$

It should be noted that the Coulomb and the nuclear fields tend to add destructively because of their opposite signs. This gives rise to Coulomb-nuclear interference. The type of collective nuclear model (vibrational or rotational)

determines the form of the interaction potential. In the rotational model, the nucleus is assumed permanently deformed, with deformation parameter β , hence its description as rotations of a non-spherical equilibrium shape. In the vibrational model, the nucleus is treated as vibrations about a spherical equilibrium shape. The nuclear interaction potential $U_N(r, \xi)$ assumes the spherical shape of the nucleus; hence, the optical potential is deformed by either vibrations about a spherical shape of radius $R_{R,I}$ or by rotations of a deformed nucleus of radius $R_{R,I}$.

A Taylor series expansion of $U_N(r, \xi)$ about $R = R_{R,I}$, neglecting the higher-order terms, gives [JA70]:

$$U_N(r, \xi) = U_N(r - R_{R,I}) - \delta R \frac{d}{dr} U_N(r - R_{R,I}) . \quad (2.27)$$

The first term of the expansion is the spherically symmetric optical potential that describes the elastic scattering, and the second is responsible for the inelastic excitation. A multipole expansion of the nuclear interaction potential gives

$$U_N(r, \xi) = \sum_{LM} U_{LM}^N(r, \xi) \left[i^L Y_{LM} \left(\hat{r} \right) \right] . \quad (2.28)$$

Using the Wigner-Eckart theorem, the nuclear interaction for a transition between nuclear states J_i and J_f for a 2^L -pole excitation gives the reduced matrix element

$$\langle J_f = L \| U_L^N(r, \xi) \| J_i = 0 \rangle \equiv U_L^N(r) = \delta_L^N \frac{dU_N(r)}{dr} , \quad (2.29)$$

for both rotational or vibrational models where $dU_N(r)/dr$ is the nuclear form factor and $J_i = 0 \rightarrow J_f = L$. The nuclear deformation length δ_L^N is defined as

$$\delta_L^N = \beta_{LR,I}^N R_{R,I} , \quad (2.30)$$

where β_{LR}^N and β_{LI}^N are the real and imaginary nuclear deformation parameters, respectively. In the collective model DWBA, the Coulomb form factor $U_L^C(r)$ is expressed as:

$$U_L^C(r) = \frac{3}{2L+1} Z_1 Z_2 e^2 \delta_L^C \begin{cases} R_C^{L-1}/r^{L+1} & , \quad r > R_C \\ r^L/R_C^{L+2} & , \quad r \leq R_C \end{cases} . \quad (2.31)$$

This expression is similar to the nuclear form factor defined by Eq. (2.29). In model analyses it is customary to set the deformation lengths equal i.e. $\delta_L^C = \delta_{LR}^N = \delta_{LI}^N$.

2.4.1 Symmetry effects in inelastic excitation cross-sections

Identical particles are indistinguishable after scattering. This is a consequence of the basic inability of an observer to know which one emerges from the scattering. Symmetrisation occurs for identical particle scattering because the scattering cross-section is always symmetric with respect to $\theta_{c.m.} = 90^\circ$. In the simplest case, the observed inelastic scattering cross-section is the incoherent addition of the cross-sections for the two possibilities, i.e.

$$\left. \frac{d\sigma}{d\Omega} \right)_{\text{inel, incoh}} = \left. \frac{d\sigma}{d\Omega}(\theta_{c.m.}) \right)_{\text{inel}} + \left. \frac{d\sigma}{d\Omega}(\pi - \theta_{c.m.}) \right)_{\text{inel}} , \quad (2.32)$$

However, following the prescription of Bass [BA80], the inelastic scattering amplitudes could be added coherently, i.e.

$$\left. \frac{d\sigma}{d\Omega} \right)_{\text{inel, coh}} \propto \left| f_{\text{inel}}(\theta_{c.m.}) + (-1)^S f_{\text{inel}}(\pi - \theta_{c.m.}) \right|^2 , \quad (2.33)$$

as in Eq. (2.21).

CHAPTER 3

Experimental details

Elastic and inelastic scattering of ${}^9\text{Be} + {}^9\text{Be}$ has been investigated using the tandem accelerator and other experimental equipment associated with the C-line of the 6 MV EN Tandem accelerator at iThemba LABS (Gauteng). This chapter presents a detailed description of the experimental techniques, the equipment and the data extraction procedures.

3.1 Experimental procedures

3.1.1 ${}^9\text{Be}$ beams

The ${}^9\text{Be}$ beam was extracted from a model 860C sputter ion source from General Ionex Corporation. The beam was extracted in the form of ${}^9\text{BeH}^-$ by bombarding caesium positive-ions onto a cylindrical target cathode made of a compressed mixture of high purity ${}^9\text{Be}$ and titanium hydride (TiH_2) powder. This led to the formation of BeH^- with BeO^- decreasing after a few hours of use, thus leaving a preponderance of BeH^- . A current of about 700 nA of BeH^- could typically be obtained from the sputter ion source. Through the inflection magnet, the ${}^9\text{BeH}^-$ ion produced undergoes energy and mass analysis in order to separate the various negative ions produced from the 860C sputter ion source, full details concerning the development of ${}^9\text{Be}$ beams can be obtained from [MA11]. After the inflection magnet, the beam was injected into the accelerator. On passing through the gas stripper channel at the centre terminal of the Tandem accelerator, the beam was stripped to predominantly ${}^9\text{Be}^{4+}$.

3.1.2 ${}^9\text{Be}$ target

The ${}^9\text{Be}$ target used in the experiment was self-supporting with an areal density of

$\approx 50 \mu\text{g}/\text{cm}^2$. The ^9Be target foil was prepared by an electron-gun evaporation of ^9Be metal. During the evaporation, the ^9Be vapour condensed onto a glass microscope slide covered with a thin layer of BaCl_2 (release agent). Therefore, ^{137}Ba constitutes the main impurity in the ^9Be target. The contaminant of ^{137}Ba in the ^9Be target produced a prominent peak in the measured energy spectra. Owing to Rutherford scattering, the prominent peak of ^{137}Ba was used for the energy calibration and normalization for integrated beam current. A current of about 5 - 20 nA electrical of $^9\text{Be}^{4+}$ was delivered on to the target at $E_{\text{Lab}}(^9\text{Be}) = 25 \text{ MeV}$ from the accelerator. Due to the toxicity of beryllium, the ^9Be target was handled with great care.

3.2 Experimental set-up

3.2.1 Scattering chamber

The small scattering chamber (20 cm diameter) located at the end of the C-line was used for the experimental work and is shown in the schematic drawing of the beam line (C-line) in Fig 3.1. It has a rotating top part which is attached to the base carrying the target holder. The target holder which accommodates up to six targets was aligned to the vertical axis of the chamber. The rotating top part of the chamber tilts out of the horizontal plane, making it possible for measurements to be taken on either side of the 0° scattering angle from $\theta_{\text{Lab}} = -20^\circ$ to $+135^\circ$.

The $^9\text{Be}^{4+}$ beam from the accelerator can be viewed on the quartz Faraday Cup 1, for alignment prior to transmission into the C-line. The quadrupole magnet focuses the beam down the C-line into the small scattering chamber through a 1 mm diameter tantalum collimator and an anti-scatter collimator to bombard the beryllium target foil.

To determine the accuracy of the absolute Lab scattering angle, a Rutherford scattering left-right asymmetry angle check was carried out at $\theta_{\text{Lab}} = +20^\circ$ and -20° , respectively. Both results were found to be within the error bars of the measurements and thus confirm the reliability of the absolute Lab scattering

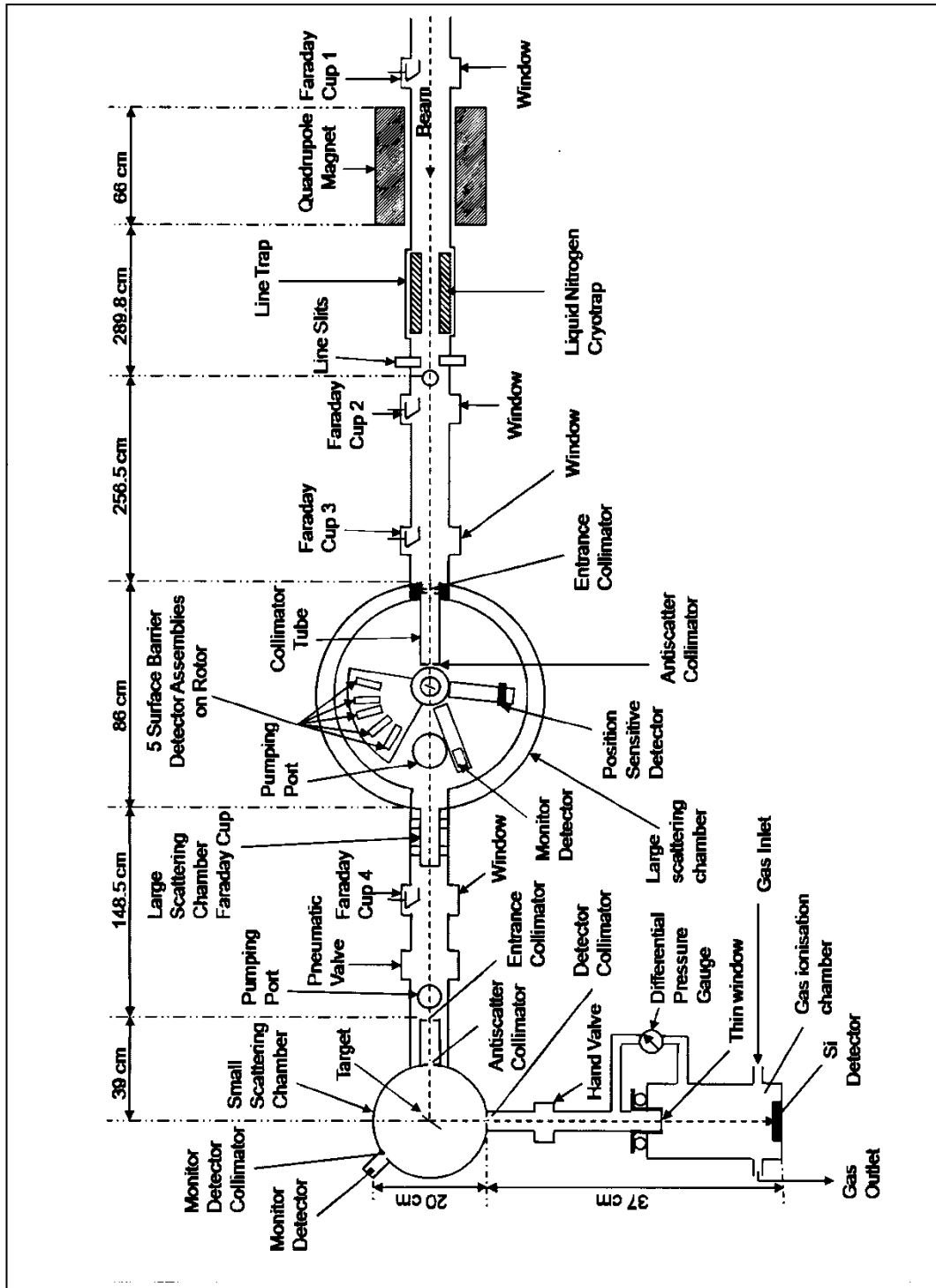


Figure 3.1: Experimental equipment associated with the C-line of the 6 MV EN Tandem accelerator at iThemba LABS (Gauteng) [JI10].

angle to $\pm 0.1^\circ$.

3.2.2 ΔE - E gas-ionisation detector

A high resolution ΔE - E gas-ionisation detector is coupled to the small scattering chamber through a port carrying the detector collimator. Figure 3.2 shows a schematic layout of the ΔE - E gas-ionisation detector. The ΔE - E gas-ionisation detector was used in the experiment to identify the scattered reaction products and determine their kinetic energies. The scattered reaction products pass through a mylar window (thickness 1 μm) and some energy (ΔE_{mylar}) is lost. Entering an iso-butane gas-filled space, it loses more energy ($\Delta E_{\text{iso-butane}}$) as a result of ionisation. The reaction products are finally brought to rest by a solid-state silicon surface barrier detector and their energy (E_{stop}) measured.

The average energy loss (stopping power) by ionisation of charged particles can be calculated using the Bethe-Bloch formula [LE92]:

$$-\frac{dE}{dx} = 2\pi N_A r_e^2 m_e c^2 \rho \frac{Zq^2}{A\beta^2} \left\{ \ln \left(\frac{2m_e \gamma^2 v^2 W_{\text{max}}}{I^2} \right) - 2\beta^2 - \delta - 2\frac{C}{Z} \right\}, \quad (3.1)$$

where

$$2\pi N_A r_e^2 m_e c^2 = 0.5135 \text{ MeVcm}^2/\text{g},$$

$-dE$ = energy lost in a distance dx ,

N_A = Avogadro's constant ($6.022 \times 10^{23} \text{ mol}^{-1}$),

r_e = the classical electron radius ($2.817 \times 10^{-13} \text{ cm}$),

m_e = the rest mass of the electron,

c = the speed of light,

ρ = the density of the absorbing material,

Z = the atomic number of the absorbing material,

A = the atomic mass of the absorbing material,

q = the charge of the incident particle in units of e

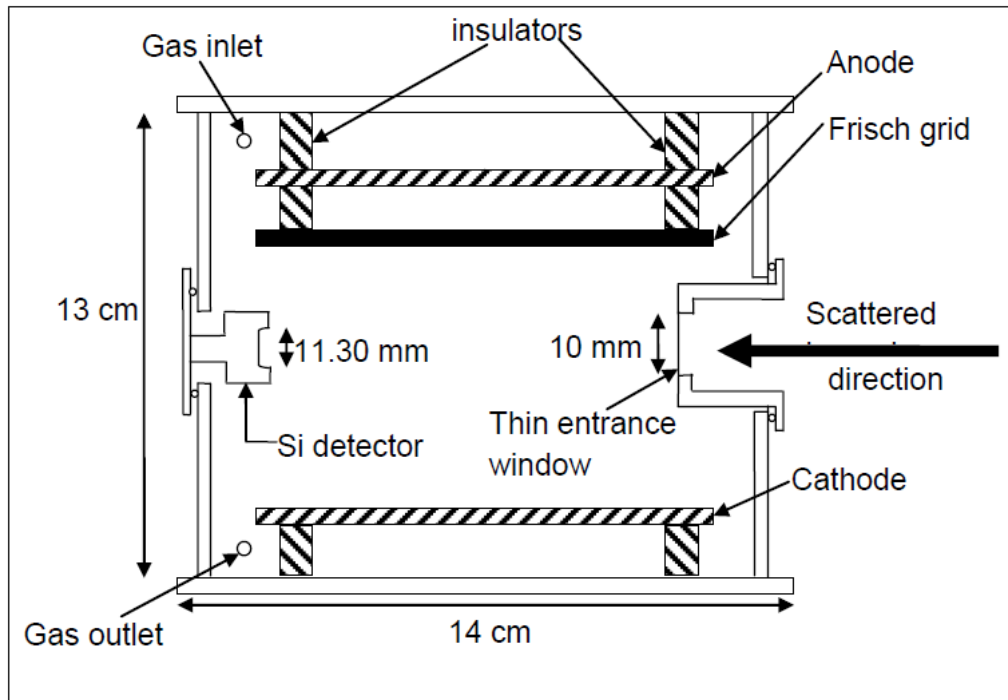


Figure 3.2: Schematic drawing of the ΔE - E gas-ionisation detector (taken from [MA11]).

$$\beta = v/c ,$$

$$\gamma = 1/\sqrt{1-\beta^2} ,$$

v = velocity of the incident particle,

W_{\max} = the maximum energy transfer in a single collision,

I = the mean excitation potential of the target,

δ = the density correction and

C = shell correction.

It should be noted that dE/dx is velocity dependent and decreases rapidly with increase in velocity because of the $1/\beta^2$ factor in Eq. (3.1). As kinetic energy increases, the factor $(1-\beta^2)$ in the logarithmic term gives dE/dx a logarithmic increase [YA61]. When the velocity of the incident particle is much less than the speed of light, Eq. (3.1) becomes

$$\frac{dE}{dx} = K \frac{mZ^2}{E}, \quad (3.2)$$

where K is a constant and m is the mass of the incident particle. Equation (3.2) implies

$$E \left(\frac{dE}{dx} \right) = KmZ^2, \quad (3.3)$$

which provides the basis for particle identification through the use of a gas-ionisation detector. The gas-ionisation chamber consists of an anode, a Frisch grid and a cathode. The signals are acquired from the anode while the Frisch grid controls the charge collection. Iso-butane gas with a regulated differential pressure of 1 kPa was used as a working gas in the ionisation chamber. The other operating conditions of the ΔE - E gas-ionisation detector were established from an experiment carried out to determine a stable plateau region for the detector's operation [JI10]. These conditions are listed in Table 3.1.

Table 3.1 Bias voltages used for the ΔE - E gas-ionisation detector [JI10].

Iso-butane Pressure (kPa)	V_C (V)	V_G (V)	V_A (V)
1 \pm 0.05	-30	+30	+230

3.2.3 Gas delivery system

The ΔE - E gas-ionisation detector gas-delivery system was mounted on a movable platform as shown in Fig. 3.3. This system was used to control and transport the iso-butane gas to the ΔE part of the ΔE - E gas-ionisation detector. The gas delivery system is made up of valves which includes; the green knob valve (isolating the active volume from the high vacuum of the scattering chamber), the floating-ball flow meter valve, the black gas valve and the backing pump valve. A high-

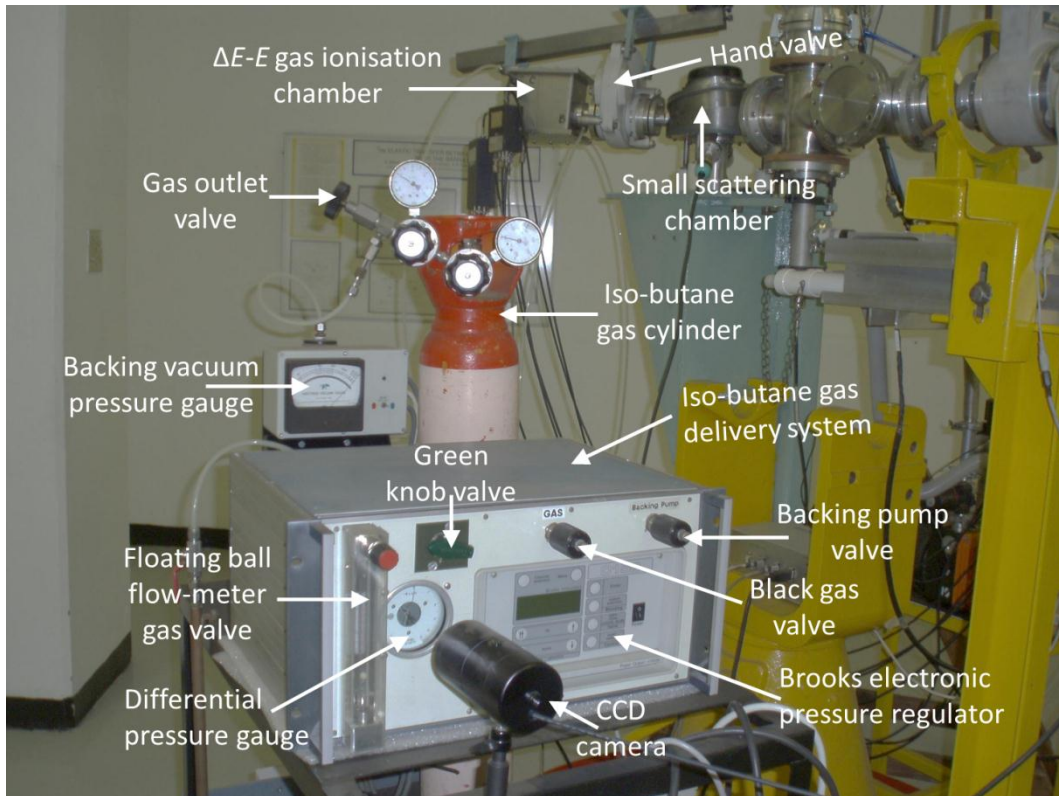


Figure 3.3: Photograph of the gas delivery system and beam line components.

precision mechanical pressure gauge was used to determine the differential pressure. The image of this from the CCD camera was viewed in the accelerator control room and was used to monitor the differential pressure, which was maintained at 1 ± 0.05 kPa by the Brooks electronic pressure regulator.

3.2.4 Electronics

Standard NIM electronic modules were used to process the signals from the detector prior to online data acquisition using a CAMAC system. The block diagram for the electronics is shown in Fig. 3.4. Signals from the detectors in the target room were boosted by the preamplifiers and then transmitted through long coaxial cables to the Data Room. The unipolar outputs after amplification were fed into the Analogue-to-Digital Converters (ADCs) via suitable delay amplifiers. The bipolar outputs were fed into the Timing Single Channel Analysers (TSCA's)

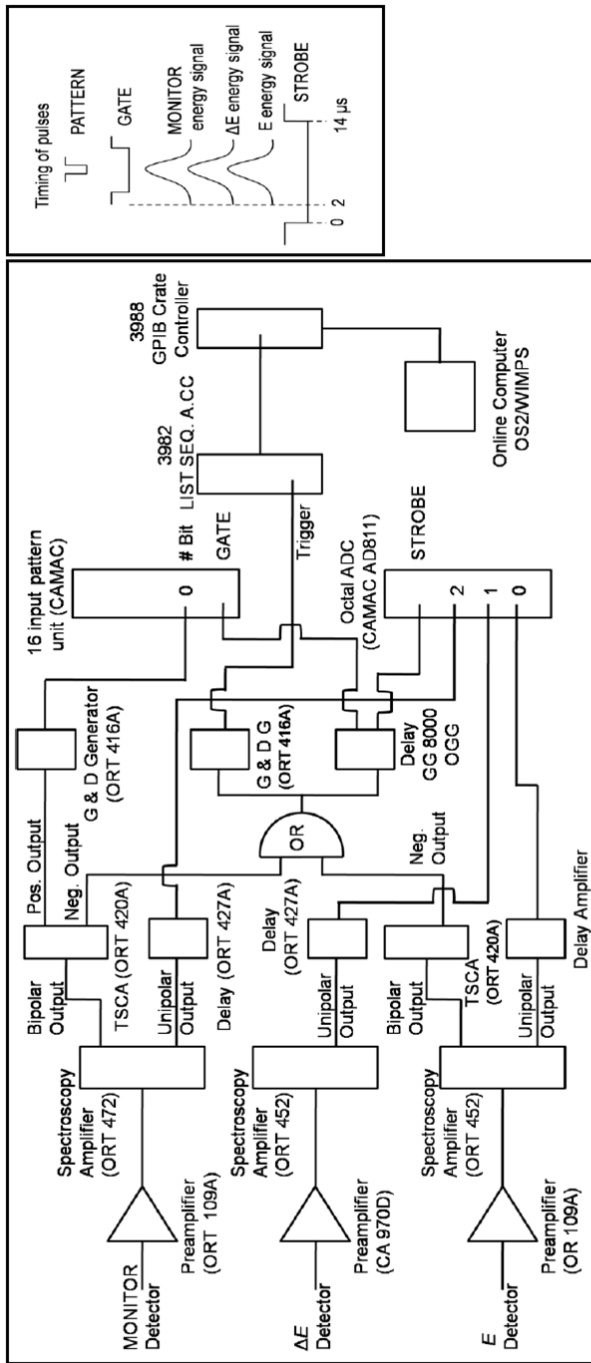


Figure 3.4: Block diagram of the electronics data acquisition system used in the ${}^9\text{Be} + {}^9\text{Be}$ measurements [KU10].

and provided inputs into the logic OR gate to determine the type of event. The Monitor, ΔE and E_{stop} signals after being brought into time coincidence were processed by the ADC's of the CAMAC data acquisition. The digital signal from the ADC's went into an online computer, which was operated with the data acquisition system WIMPS OS/2 [FE92].

3.3 Data collection and extraction

The digitized information from the ADC's of the CAMAC data acquisition system were stored in the computer buffers in the form of singles spectra ΔE , E_{stop} and E_{monitor} together with a two dimensional ΔE - E_{stop} spectrum. For each scattering angle, a ΔE - E_{total} spectrum was obtained. The total kinetic energy E_{total} is given as $E_{\text{total}} = E_{\text{stop}} + n\Delta E$, where n is a factor which normalised the ΔE signal to the E_{stop} signal. The value for the normalisation factor was determined to be $n = 0.261$, by relating the corresponding E_{stop} signals at $\theta_{\text{Lab}} = 25^\circ$ for the ΔE gas-ionisation chamber GAS ON and GAS OFF settings. A typical measured two-dimensional ΔE - E_{total} spectrum obtained during the experiment is shown in Fig. 3.5, with the ${}^9\text{Be}$ events clearly separated from carbon and helium products.

From the measured two dimensional ΔE - E_{total} spectrum the part corresponding to ${}^9\text{Be}$ in Fig. 3.5 was projected onto the x-axis and transformed into the one-dimensional E_{total} spectrum shown in Fig. 3.6. Several peaks can be seen in the energy spectrum of Fig. 3.6. Peaks denoted by ${}^9\text{Be}$ and ${}^9\text{Be}'$ correspond to the ground state and 2.43 MeV excited state of ${}^9\text{Be}$, respectively. Below channel 140 lies a continuum of smoothly varying background. Other peaks denoted by ${}^{12}\text{C}$, ${}^{16}\text{O}$, ${}^{35}\text{Cl}$ and ${}^{137}\text{Ba}$ indicate scattering from the target contaminants.

The ${}^9\text{Be}$ elastic and inelastic scattering peaks identified for each scattering angle were fitted using a Gaussian function with a linear background. The formula used is given by

$$y(x) = b + h \exp \left\{ -0.5 \left(\frac{x - x_0}{\sigma} \right)^2 \right\}, \quad (3.4)$$

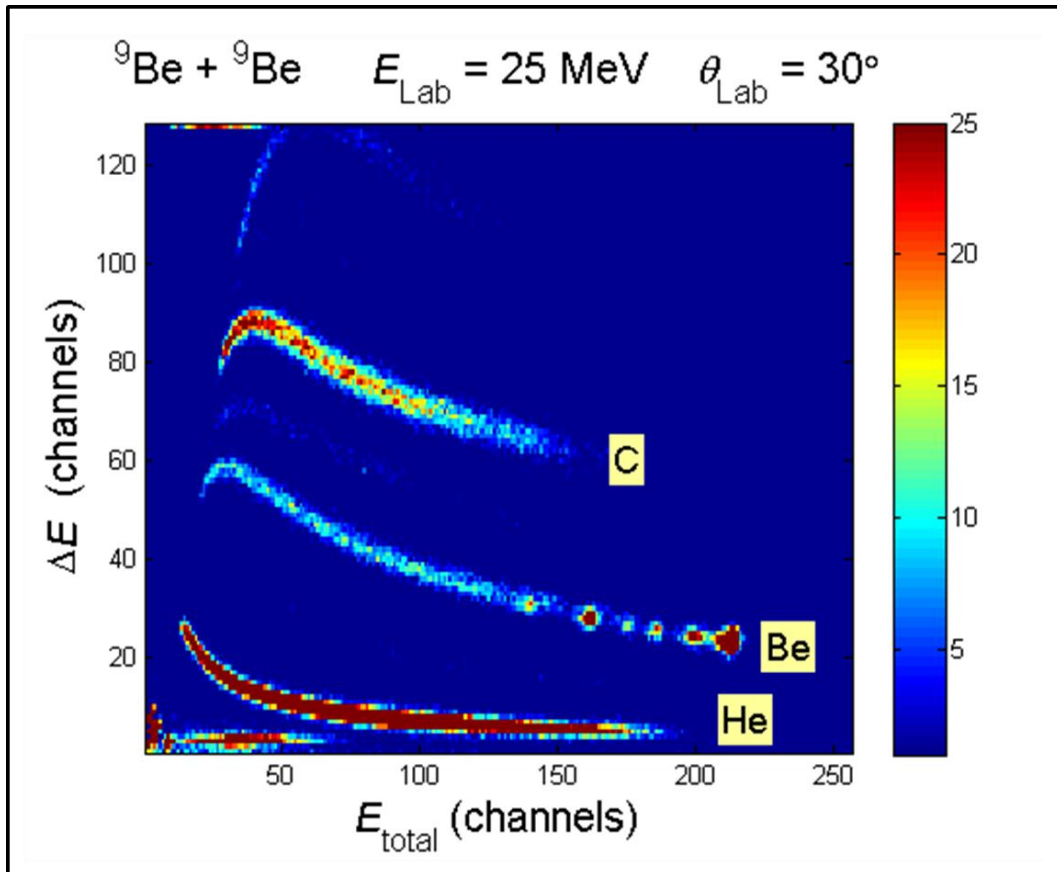


Figure 3.5: Two dimensional ΔE - E_{total} spectrum for ${}^9\text{Be} + {}^9\text{Be}$ at $E_{\text{Lab}}({}^9\text{Be}) = 25$ MeV and $\theta_{\text{Lab}} = 30^\circ$.

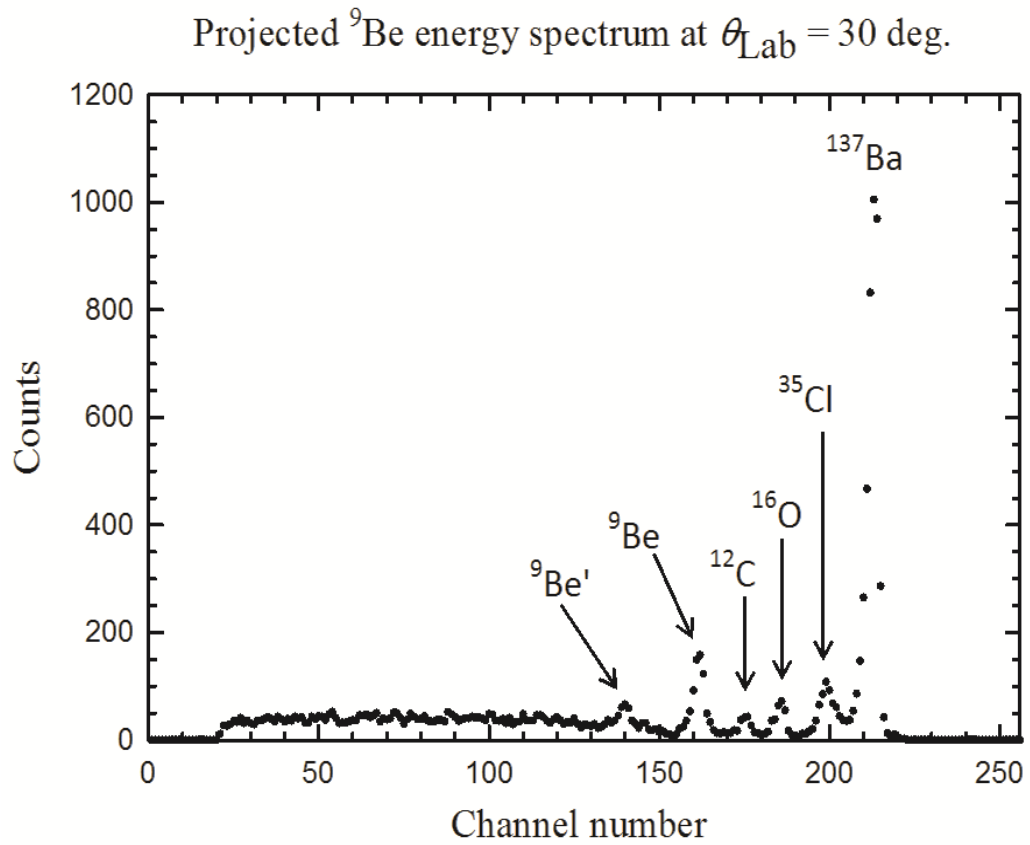


Figure 3.6: Transformed and projected one dimensional ΔE - E_{total} spectrum of ${}^9\text{Be}$ + ${}^9\text{Be}$ at $E_{\text{Lab}}({}^9\text{Be}) = 25$ MeV and $\theta_{\text{Lab}} = 30^\circ$.

where b is the linear background defined as $b = a_0 + a_1x$, h is the peak height, x is the channel number, x_0 is the peak centroid and σ is the standard deviation. The same value of standard deviation determined for the elastic scattering peak was used for the inelastic scattering peak at the same scattering angle, it was sufficient to employ a linear background.

The area A under the Gaussian peak fit was determined using the expression

$$A = h\sigma\sqrt{2\pi}, \quad (3.5)$$

with the total area A_T under the peak being expressed as

$$A_T = A + B, \quad (3.6)$$

where B is the background under the peak

The error ΔA on the extracted peak area is given by

$$\Delta A = \chi^2 \sqrt{(A+B) + B}. \quad (3.7)$$

Here, the minimum reduced - χ^2 is defined as

$$\chi^2 = \frac{1}{N} \sum_i \left[\frac{y_i - y(x_i)}{\alpha_i} \right]^2, \quad (3.8)$$

where $\alpha_i = (y_i)^{\frac{1}{2}}$ are the uncertainties on the data points y_i and N is the number of degrees-of-freedom, that is the number of variable parameters subtracted from the number of data points [CA78]. Generally, it was found that $\chi^2 < 1$ resulted from the fitting procedure.

It should be noted that when the background B is small, Eq. (3.7) reduces to

$$\Delta A = \sqrt{A}, \quad (3.9)$$

as expected.

3.4 Evaluation of scattering cross-sections

To determine the elastic and inelastic scattering cross-sections, the following steps were taken:

1. The elastic and inelastic scattering yields were obtained using the fitting procedure outlined in Section 3.3.
2. For each scattering angle measured, the monitor detector yield was obtained from the monitor detector energy spectrum (by way of example see Fig. 3.7).
3. The monitor detector yields were normalised at $\theta_{\text{Lab}} = 25^\circ$.
4. The Lab yield and the normalised monitor detector yield were multiplied together to give normalised Lab yield.
5. The respective Lab to c.m. kinematic factors were multiplied into the normalised Lab yield to give the normalised yield in the centre-of-mass reference frame using [MA68]:

$$I(\theta_{\text{c.m.}}) = I(\theta_{\text{Lab}}) \left(\frac{\sin^2 \theta_{\text{Lab}}}{\sin^2 \theta_{\text{c.m.}}} \right) \cos(\theta_{\text{c.m.}} - \theta_{\text{Lab}}), \quad (3.10)$$

where $I(\theta_{\text{c.m.}})$ is the intensity at each scattering angle $\theta_{\text{c.m.}}$ in the centre-of-mass reference frame and $I(\theta_{\text{Lab}})$ is the intensity at each scattering angle θ_{Lab} in the laboratory frame.

6. In the first instance, absolute scattering cross-sections were obtained for each scattering angle by referencing to the optical model prediction at the most forward scattering angle $\theta_{\text{Lab}} = 12.5^\circ$ ($\theta_{\text{c.m.}} = 25^\circ$).

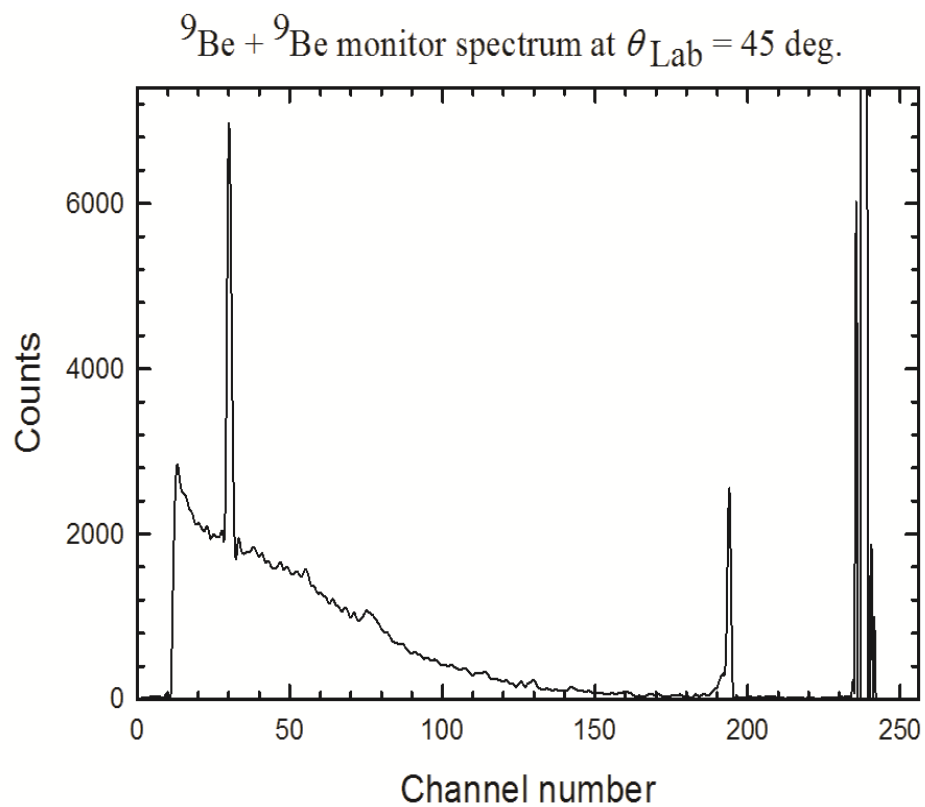


Figure 3.7: One dimensional monitor detector spectrum for ${}^9\text{Be} + {}^9\text{Be}$ at $E_{\text{Lab}}({}^9\text{Be}) = 25$ MeV and $\theta_{\text{Lab}} = 45^\circ$.

7. The ratio to Mott scattering cross-sections for each scattering angle were obtained. The numerical values obtained are shown in Table A1 in the Appendix section.

8. The counting statistics error, the error in summing the peaks and the percentage errors in the Gaussian peak fitting constitutes the major error in these measurements (see Eqs. (3.7) and (3.9)).

CHAPTER 4

Analysis and discussion

Angular distributions at $E_{\text{Lab}}(^9\text{Be}) = 25$ MeV have been measured for the elastic scattering and inelastic excitation to an unbound state in the fermionic system $^9\text{Be} + ^9\text{Be}$. In this chapter, previous data on $^9\text{Be} + ^9\text{Be}$ scattering [MA11] are reviewed and the effect of intrinsic spin on the interference term of Mott scattering is illustrated. The present data for the elastic and inelastic scattering are analysed in terms of the Optical Model (OM) and the Distorted Wave Born approximation (DWBA), respectively.

4.1 Review of $^9\text{Be} + ^9\text{Be}$ scattering and rationale for data collection

Elastic scattering and inelastic excitation of the second, unbound, state ^9Be ($5/2^-$, 2.430 MeV) has been studied recently [MA11] for the fermionic $^9\text{Be} + ^9\text{Be}$ system at energies close to and well above the Coulomb barrier. By way of example, Fig. 4.1 shows excitation function measurements and Fig. 4.2 angular distributions taken from Ref. [MA11]. An energy-independent optical model potential was obtained from fits to the measured elastic scattering data in this work. The corresponding optical model predictions are shown in Figs. 4.1 and 4.2 (denoted as “W-4 Pot. OM” in the figures). As can be seen, excellent fits to the elastic scattering data were obtained over an energy range $3 \text{ MeV} \leq E_{\text{Lab}}(^9\text{Be}) \leq 25 \text{ MeV}$. These data extend the limited existing data of York and Carpenter [YO77] and demonstrate that an energy-dependent optical potential is not required. In addition, a DWBA analysis was performed using the W-4 potential for the inelastic excitation of the second, unbound, state ^9Be ($5/2^-$, 2.43MeV) at $E_{\text{Lab}}(^9\text{Be}) = 16$ MeV [MA11], which was treated as a $\Delta L = 2$ h transition from the ground

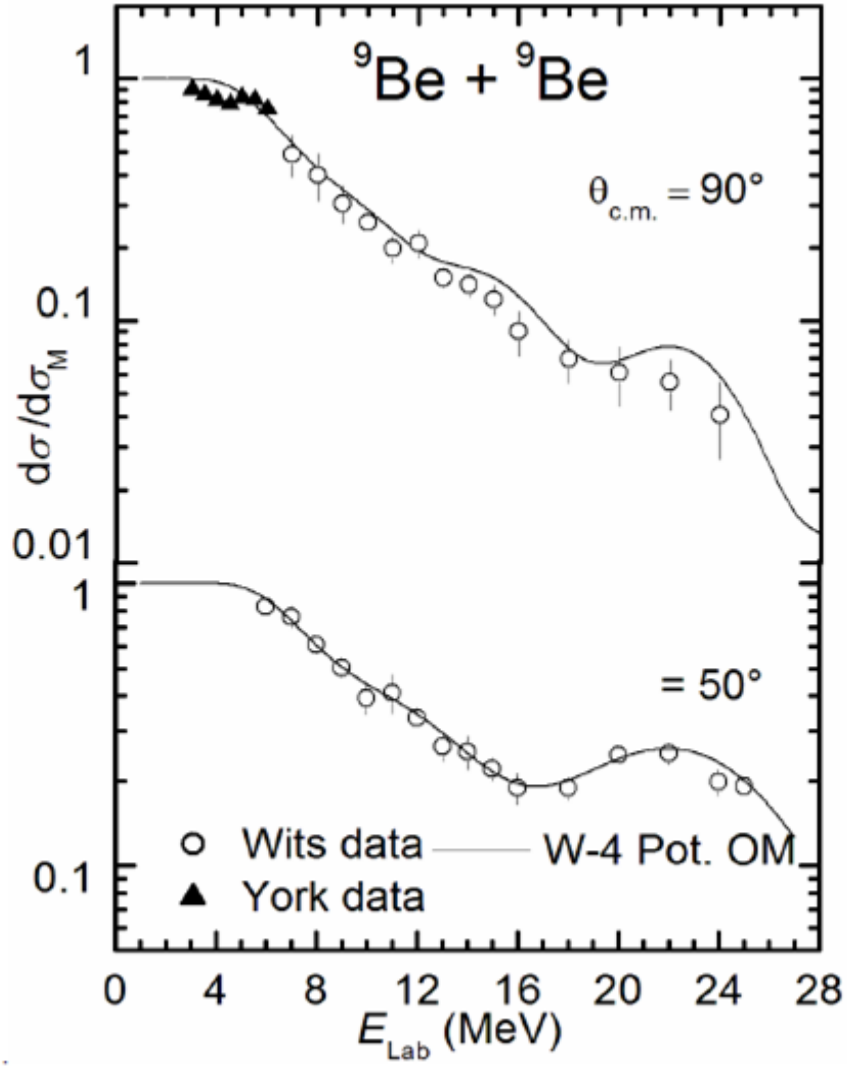


Figure 4.1: *Upper part:* Excitation function for the elastic scattering of ${}^9\text{Be} + {}^9\text{Be}$ at $\theta_{\text{c.m.}} = 90^\circ$ for $E_{\text{Lab}}({}^9\text{Be}) = 3$ to 24 MeV. *Lower part:* Excitation function for the elastic scattering of ${}^9\text{Be} + {}^9\text{Be}$ at $\theta_{\text{c.m.}} = 50^\circ$ for $E_{\text{Lab}}({}^9\text{Be}) = 6$ to 25 MeV. Note that kinematically measurements can be made at an angle $\theta_{\text{Lab.}} = 25^\circ$ only down to $E_{\text{Lab}}({}^9\text{Be}) = 6.0$ MeV (taken from [MA11]).

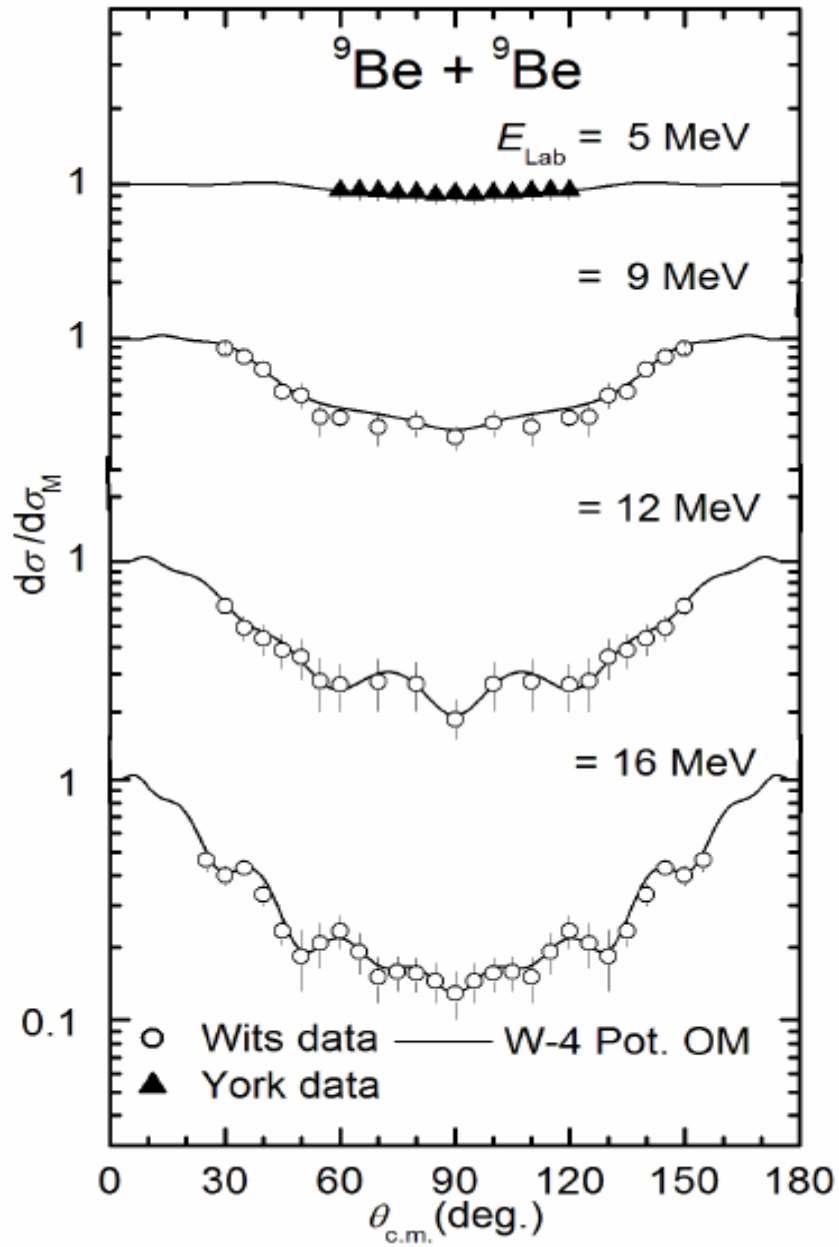


Figure 4.2: Angular distributions for the elastic scattering of ${}^9\text{Be} + {}^9\text{Be}$ at $E_{\text{Lab}}({}^9\text{Be}) = 5 \text{ MeV}, 9 \text{ MeV}, 12 \text{ MeV}$ and 16 MeV (taken from [MA11]).

state ${}^9\text{Be}$ ($3/2^-$, g.s.), the results of which are also shown in Fig 4.3. As can be seen in Fig. 4.3, the elastic scattering data are symmetric around $\theta_{\text{c.m.}} = 90^\circ$, as expected for identical particle scattering. However, due to the limited nature of the inelastic scattering data at backward scattering angles, symmetry effects cannot be distinguished. Here, measurement was limited by the low energy cut-off imposed by the ΔE - E gas-ionisation detector system. We, therefore, used in this study the highest incident beam-energy presently available $E_{\text{Lab}}({}^9\text{Be}) = 25$ MeV in order to extend the backward scattering angle measurements. The rated maximum beam energy for the EN Tandem of $E_{\text{Lab}}({}^9\text{Be}) = 29$ MeV unfortunately was not achievable. Corresponding DWBA predictions are shown in Fig. 4.4 where the vertical arrows indicate the expected instrumental cut-offs (discussed below). Because of the low energy of the inelastically scattered ${}^9\text{Be}$ detected at $E_{\text{Lab}}({}^9\text{Be}) = 16$ MeV, the inelastic excitation of the second, unbound, state in ${}^9\text{Be}$ ($5/2^-$, 2.43 MeV) could not be measured beyond $\theta_{\text{c.m.}} = 102^\circ$ (shown by the thick arrow in Fig. 4.4).

In order to access more backward scattering angles for the inelastic state of interest, energy loss calculations [JI84] were made to determine the cut-off angles for a scattered ${}^9\text{Be}$ particle which for the measurements in Ref. [MA11] was $E_{\text{Lab}}({}^9\text{Be}') = 5.2$ MeV. With the existing configuration for the gas-ionisation detector of a 1 μm thick mylar entrance window and 1 kPa iso-butane differential gas pressure (see Section 3.2.2), the kinetic energy cut-off angle resulting from the scattered ${}^9\text{Be}$ is shown in Table 4.1. However, using a configuration of 0.5 μm mylar and 1 kPa iso-butane differential gas pressure, the kinematic cut-off angle as a result of the scattered ${}^9\text{Be}$ is also shown in Table 4.1. Thus, it can be seen that the change in scattering angle between going from 1 μm to 0.5 μm thick mylar is very small (approximately 3° in the centre-of-mass). As such, it was decided not to reduce the thickness of the mylar entrance window to the gas-ionisation detector which would also reduce the strength and safety of the window.

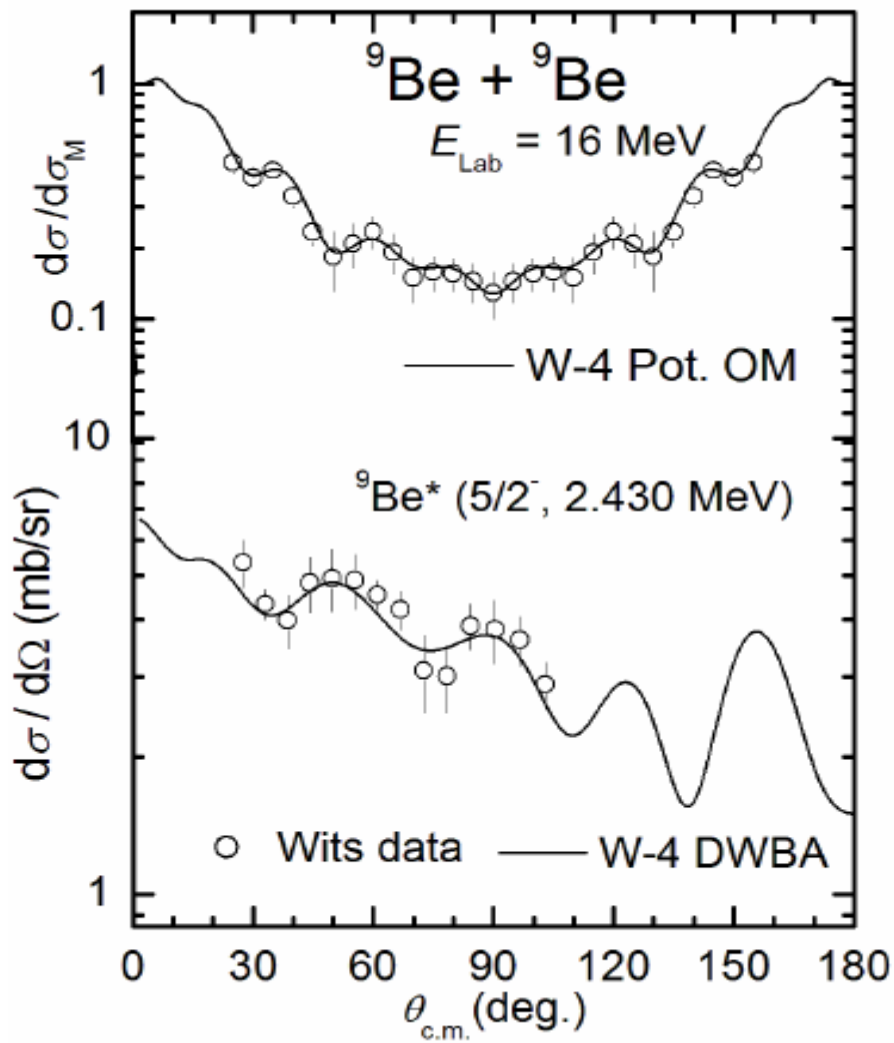


Figure 4.3: *Upper part:* Angular distributions for the elastic scattering of ${}^9\text{Be} + {}^9\text{Be}$ at $E_{\text{Lab}} = 16 \text{ MeV}$. *Lower part:* Inelastic excitation of the second, unbound, state in ${}^9\text{Be}$ ($5/2^-, 2.43 \text{ MeV}$) at $E_{\text{Lab}} = 16 \text{ MeV}$ (taken from [MA11]).

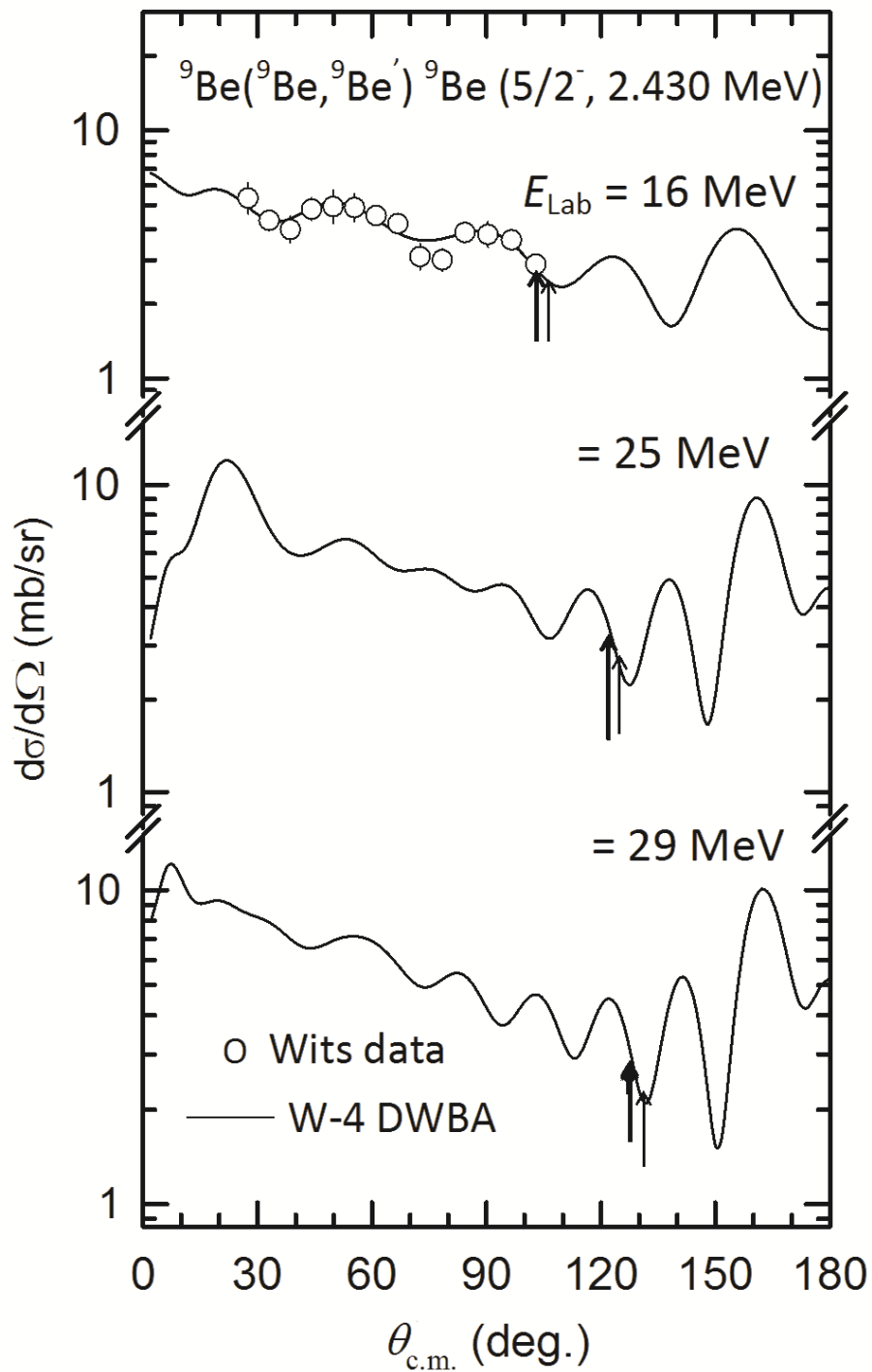


Figure 4.4: Inelastic excitation of the second, unbound, state ${}^9\text{Be} (5/2^-, 2.43 \text{ MeV})$ at $E_{\text{Lab}}({}^9\text{Be}) = 16 \text{ MeV}$, 25 MeV and 29 MeV . Thick vertical arrows show the cut-off angle with a $1 \mu\text{m}$ thick mylar entrance window. Thin vertical arrows show the cut-off angle with a $0.5 \mu\text{m}$ thick mylar entrance window.

Table 4.1 Inelastic scattering cut-off angle with an entrance window for the ΔE - E gas-ionisation detector system of 1 μm and 0.5 μm thick mylar and 1 kPa isobutane differential pressure for various incident ${}^9\text{Be}$ beam energies.

$E_{\text{Lab}} ({}^9\text{Be})$ (MeV)	<u>1 μm mylar</u>		<u>0.5 μm mylar</u>	
	θ_{Lab}	$\theta_{\text{c.m.}}$	θ_{Lab}	$\theta_{\text{c.m.}}$
	(deg.)	(deg.)	(deg.)	(deg.)
16	45	102.9	46.2	106.0
25	55	120.9	56.3	124.4
29	58	126.4	59.0	129.1

Figure 4.5 shows the energy levels of ${}^9\text{Be}$, with most low-lying levels belonging to either a $I^\pi = 3/2^-$ or a $I^\pi = 1/2^+$ rotational states [KU60]. The inelastic excitation proceeds strongly from ${}^9\text{Be}$ ($3/2^-$, g.s.) to the second, unbound, state ${}^9\text{Be}$ ($5/2^-$, 2.43 MeV) involving an angular momentum $\Delta L = 2 \hbar$ ($E2$). The ${}^9\text{Be}$ breaks up with ease into $n + 2\alpha$ at excitation energy $E_x = 1.5735$ MeV. Therefore, inelastic excitation to the ${}^9\text{Be}$ ($5/2^-$, 2.43 MeV) state proceeding as a two-body interaction allows the inelastically scattered ${}^9\text{Be}$ to be detected with the excited state breaking up sometime later after the interaction.

4.2 Identical particle scattering and intrinsic spin

Identical particle scattering is described by the Mott scattering (see Section 2.1.2). The nature of the third term (interference term) of the Mott scattering formula Eq. (2.4) is dependent on the intrinsic spin I of the ground state. The value of spin determines the statistics of many identical particle systems. The sensitivity of the

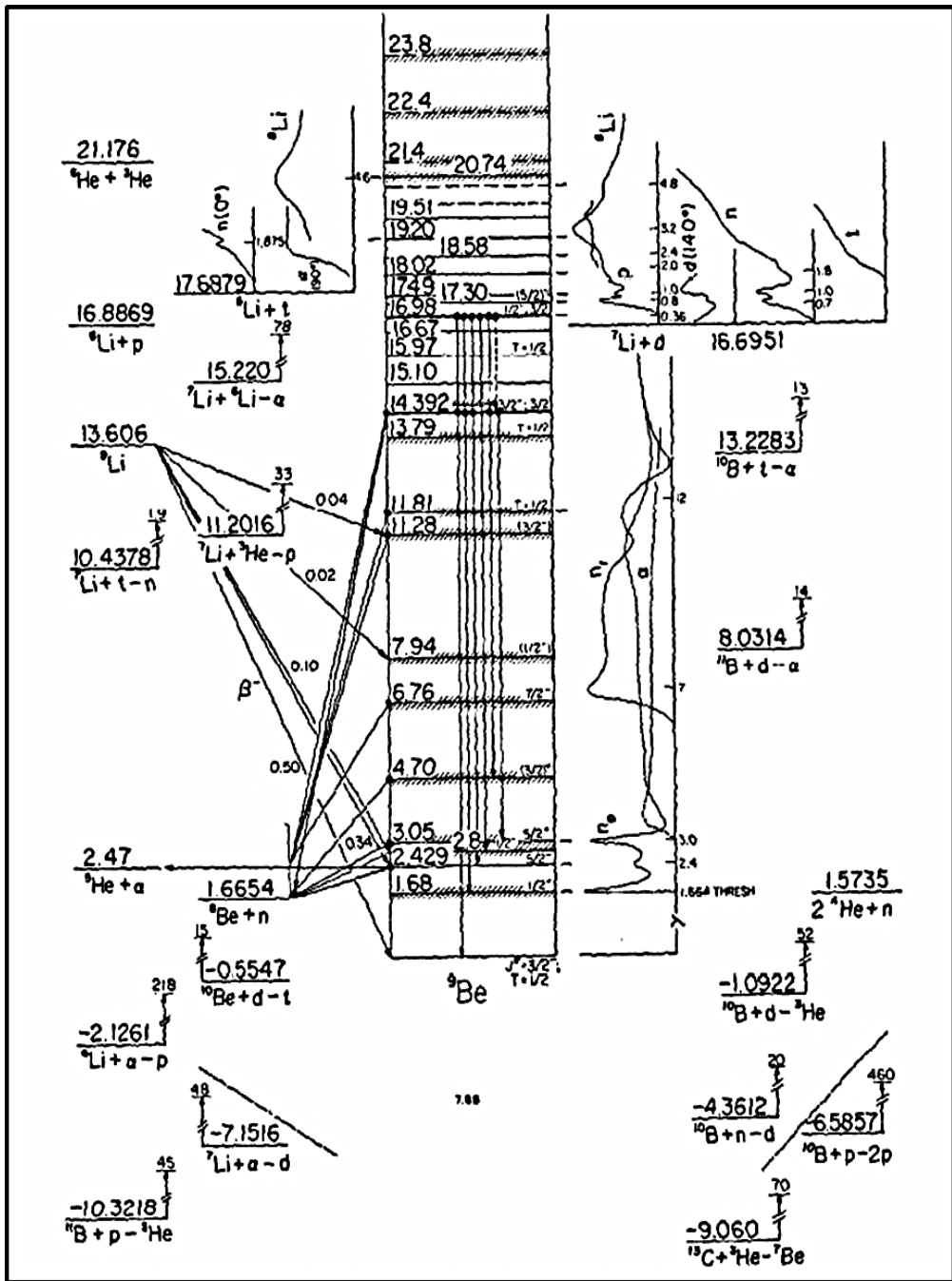


Figure 4.5: Energy levels of ${}^9\text{Be}$ [AJ88].

interference term to the intrinsic spin value is demonstrated in Fig. 4.6. Here, it can be clearly seen that the Mott scattering cross-section is symmetric with respect to $\theta_{c.m.} = 90^\circ$, as it must be for identical particles. As seen from Eq. (2.4), the interference term becomes smaller for large values of intrinsic spin I , hence, for fermionic systems (half-integer spin) as spin I increases the Mott cross-section tends towards a maximum at around $\theta_{c.m.} = 90^\circ$.

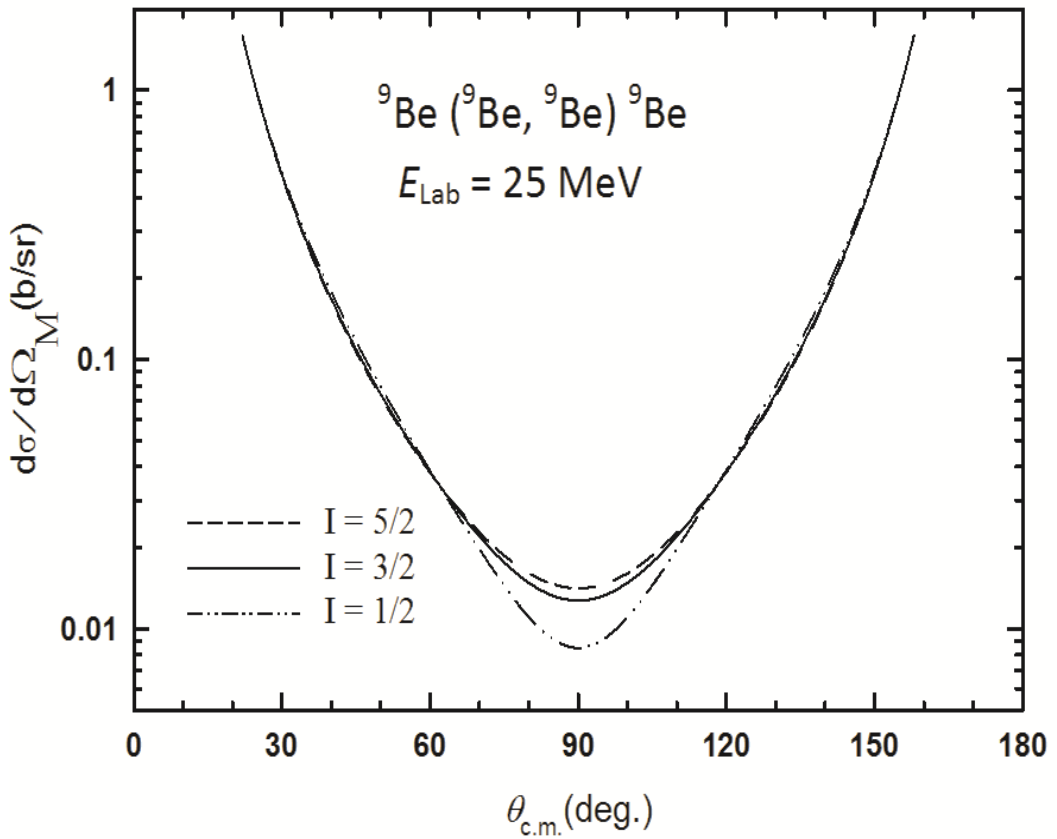


Figure 4.6: Angular distributions for ${}^9\text{Be} + {}^9\text{Be}$ Coulomb scattering at $E_{\text{Lab}}({}^9\text{Be}) = 25 \text{ MeV}$, assuming different intrinsic spin values I .

4.3 Elastic and inelastic scattering of ${}^9\text{Be} + {}^9\text{Be}$ at $E_{\text{Lab}}({}^9\text{Be}) = 25 \text{ MeV}$

Elastic and inelastic-scattering angular distributions for ${}^9\text{Be} + {}^9\text{Be}$ were measured at $E_{\text{Lab}}({}^9\text{Be}) = 25 \text{ MeV}$. The elastic scattering data were measured for $25.0^\circ \leq \theta_{\text{c.m.}} \leq 125.0^\circ$ while the inelastic scattering cross-sections were in the range $26.5^\circ \leq \theta_{\text{c.m.}} \leq 134.8^\circ$ (see Table 4.2). These measurements were made in angular steps of $\Delta\theta_{\text{Lab}} = 2.5^\circ$.

4.3.1 Review of the measured data

In this study, we present new measurements of the elastic and inelastic scattering of the ${}^9\text{Be} + {}^9\text{Be}$ system. An overview of the measured data is given in Table 4.2. An Optical Model (OM) analysis was performed for the elastic-scattering angular distribution and the ratio to Mott determined. Absolute cross-sections were obtained by normalizing the elastic scattering data to the calculated optical model prediction at the most forward scattering angle $\theta_{\text{c.m.}} = 25^\circ$. The measured absolute cross-sections divided by the Mott cross-section were calculated with corresponding errors, and are shown in the top part of Fig. 4.7 (for the sake of intercomparison, all of the figures for this section are placed together at the end of the section). Here, the measured cross-sections are shown by open and filled circles. The open circles for $\theta_{\text{c.m.}} > 90^\circ$ are the mirror reflections of the $\theta_{\text{c.m.}} < 90^\circ$ data plotted as a function of $(\pi - \theta_{\text{c.m.}})$. It can be seen that the independently-measured elastic scattering cross-sections for $\theta_{\text{c.m.}} > 90^\circ$ ($\theta_{\text{c.m.}} = 2\theta_{\text{Lab}} (> 45^\circ)$ shown by the filled circles) correspond very well with the mirrored data points. Also, the data show strong oscillatory structure. It should be noted that there is no clear minimum at $\theta_{\text{c.m.}} = 90^\circ$ because of significant compound nucleus formation and decay back to the elastic scattering channel. This has also been seen in the corresponding data of Ungricht *et al.* [UN79]. However, since such compound nucleus decay cross-sections are isotropic about $\theta_{\text{c.m.}} = 90^\circ$ they become rapidly insignificant for the elastic scattering channel at scattering angles away from $\theta_{\text{c.m.}}$

Table 4.2 Summary of the measured data for ${}^9\text{Be} + {}^9\text{Be}$ scattering at $E_{\text{Lab}}({}^9\text{Be}) = 25 \text{ MeV}$ taken in steps of $\Delta\theta_{\text{Lab}} = 2.5^\circ$.

Outgoing channel for $E_{\text{Lab}}({}^9\text{Be}) = 25 \text{ MeV}$	Detected nucleus	θ_{Lab} (deg.)	$\theta_{\text{c.m.}}$ (deg.)
${}^9\text{Be}(3/2^-, \text{g.s.}) + {}^9\text{Be}(3/2^-, \text{g.s.})$	${}^9\text{Be}$	12.5 – 62.5	25.0 – 125.0
${}^9\text{Be}'(3/2^-, \text{g.s.}) + {}^9\text{Be}^*(5/2^-, 2.43 \text{ MeV})$	${}^9\text{Be}'$	12.5 – 60.0	26.5 – 134.8

$= 90^\circ$ for identical-particle scattering system. The calculation of compound nucleus decay cross-section is, unfortunately, beyond the scope of the present analysis. Turning now to the inelastic scattering data, this was limited to a maximum scattering angle of $\theta_{\text{c.m.}} = 134.8^\circ$, because of the low energy cut-off of the detected scattered ${}^9\text{Be}'$. Indeed, by careful adjustment of the lower-level discriminator for the ΔE - E gas-ionisation detector it turned out that measurements could be extended by almost another fourteen degrees from the expected $\theta_{\text{c.m.}} = 120.9^\circ$ (see Table 4.1). The inelastic scattering data are shown in the lower part of Fig. 4.7, again with open circles ($\theta_{\text{c.m.}} \leq 90^\circ$) and filled circles ($\theta_{\text{c.m.}} > 90^\circ$).

4.3.2 Optical model analysis of elastic scattering

The ${}^9\text{Be} + {}^9\text{Be}$ elastic scattering data were analysed in terms of the optical model by using a modified version of the code A-THREE [AU78]. The parameters of the optical model used are given in Table 4.3. The energy-independent optical model potential W-4 used was obtained from a previous fit analysis which minimized simultaneously the value of the mean square deviation, χ^2 , for all the angular distributions, see Fig. 4.2 [MA11]. The same geometry of $R_{\text{OR}} = R_{\text{OI}} = 1 \text{ fm}$ and $a_{\text{R}} = a_{\text{I}} = 0.632 \text{ fm}$ used by York and Carpenter [YO77] was used. The Coulomb radius $R_{\text{C}} = 3.23 \text{ fm}$ used was determined from electron scattering [SA80]. As can

Table 4.3 The optical model parameters for ${}^9\text{Be} + {}^9\text{Be}$ [MA11].

System	Set	V_0 (MeV)	R_{0R} (fm)	a_R (fm)	W_0 (MeV)	R_{0I} (fm)	a_I (fm)	R_C (fm)
${}^9\text{Be} + {}^9\text{Be}$	W-4	155.09	1.0	0.632	34.12	1.0	0.632	3.23

be seen in Fig. 4.7, the calculation of the elastic-scattering angular distribution with the optical model using the energy-independent potential gave a very satisfactory fit to the measured elastic scattering data. The symmetry around $\theta_{c.m.} = 90^\circ$ which is expected of identical particle scattering is clearly present both in the measured data and the model predictions. It should be noted that the W-4 optical potential also gave excellent fits to the data of ref. [UN79].

4.3.3 Distorted Wave Born Approximation (DWBA) analysis of inelastic scattering

Inelastic scattering to the second, unbound, state in ${}^9\text{Be}$ ($5/2^-$, 2.43 MeV) was calculated with the distorted wave code DWIS [VI74], a modified version of the DWUCK by P. D. Kunz. In these calculations, 400 partial waves are allowed with the radial wave-functions integrated out to 75 fm. This allows an approximation to be used for the contribution from high partial-waves where Coulomb excitation dominates. The same optical potential parameters used in the elastic scattering were used for the inelastic scattering calculations.

In Fig. 4.7, a fit to the inelastic scattering data was obtained by varying the Coulomb and the nuclear deformation parameters β_2^C and β_2^N while holding the Coulomb and the nuclear deformation length equal i.e. $\delta_2^C = \delta_2^N$. For the $3/2^- \rightarrow 5/2^-$ transition of ${}^9\text{Be}$, the results of DWIS calculation require multiplying β_2^C and β_2^N by the corresponding Clebsch-Gordon coefficient (value of 0.717). The

Coulomb deformation parameter β_2^C was determined from the relation $\beta_2^N R_R = \beta_2^C R_C$. This corresponds to $\beta_2^C = 0.1037$ and $\beta_2^N = 0.0805$. Here, as can be seen, the DWBA calculations yielded a reasonable description of the inelastic-scattering angular distribution. However, in order to fit the ${}^9\text{Be}$ ($5/2^-$, 2.43 MeV) data, a value of deformation parameter less than that used in previous analysis at $E_{\text{Lab}}({}^9\text{Be}) = 16$ MeV [MA11] was required. The values for the deformation parameters used in these calculations are shown in Table 4.4.

Table 4.4 Deformation parameters for inelastic scattering from ${}^9\text{Be}$ ($3/2^-$, g.s) to the second, unbound, state ${}^9\text{Be}$ ($5/2^-$, 2.43 MeV).

System	$E_{\text{Lab}}({}^9\text{Be})$ (MeV)	β_2^C	β_2^N	$\delta_2^C = \delta_2^N$ (fm)
${}^9\text{Be} + {}^9\text{Be}$	16 ^{a)}	0.2013	0.1562	0.65
${}^9\text{Be} + {}^9\text{Be}$	25 ^{b)}	0.1037	0.0805	0.33

^{a)} Values from Ref. [MA11].

^{b)} Present work.

The lower part of Fig. 4.8, like that of Fig. 4.7, shows additionally the inelastic scattering cross-sections calculated assuming inelastic excitation by the Coulomb interaction only and also by the nuclear interaction only.

In order to investigate symmetry effects, the lower part of Fig. 4.9 shows the inelastic scattering cross-section calculated by adding incoherently the cross-sections for the two possibilities that result during the scattering of two identical particles (see Section 2.4.1). The measured data were also reflected around $\theta_{\text{c.m.}} = 90^\circ$. A fit to the inelastic scattering data was obtained by again requiring $\beta_2^N R_R = \beta_2^C R_C$ while varying both β_2^N and β_2^C .

The lower part of Fig. 4.10 shows the inelastic scattering cross-section calculated by adding coherently the two corresponding scattering amplitudes that result from the scattering of two identical particles (also see Section 2.4.1). The measured cross-sections were also reflected around $\theta_{c.m.} = 90^\circ$. A fit to the inelastic scattering data was obtained by again requiring $\beta_2^N R_R = \beta_2^C R_C$ while varying both β_2^N and β_2^C .

4.4 Discussion

It has been shown that the measured elastic scattering data for ${}^9\text{Be} + {}^9\text{Be}$ at $E_{\text{Lab}}({}^9\text{Be}) = 25 \text{ MeV}$ can be fitted with the energy-independent optical model potential W-4 (see Fig. 4.7). The required angular symmetry around $\theta_{c.m.} = 90^\circ$ is fulfilled within the limits of error. As noted previously, the data points close to $\theta_{c.m.} = 90^\circ$ show a maximum rather than the minimum predicted by the optical model. This indicates a contribution from the compound nucleus formation and decay back to the entrance channel. Because of the isotropic nature of the compound nucleus contribution, data on either side away from the minimum at $\theta_{c.m.} = 90^\circ$ are not affected and hence are described well by the optical model.

The optical model parameters (see Table 4.3) used for elastic scattering were employed in fitting the inelastic scattering data using a one-step DWBA calculation. The results are shown in Fig. 4.7. This was found to give a good fit to the inelastic excitation to the second, unbound, state ${}^9\text{Be} (5/2^-, 2.430 \text{ MeV})$. In this regard, the nuclear inelastic excitation (shown by long dashed line) in Fig. 4.8 predicts well the gross structure of the data for the reaction leading to the excited state ${}^9\text{Be} (5/2^-, 2.43 \text{ MeV})$. However, the Coulomb inelastic excitation (shown by dash-dot-dot line) also in Fig. 4.8 is remarkably weak and does not contribute significantly to the measured cross-sections. In the case of ${}^9\text{Be} (5/2^-, 2.430 \text{ MeV})$ excitation, a deformation length of value $\delta_2 = 0.33 \text{ fm}$ was extracted., being very close to $\delta_2 = 0.36 \text{ fm}$ obtained from a coupled-channels analysis of ${}^9\text{Be} + {}^9\text{Be}$ at much higher beam energies [OM84]. However, a higher value of $\delta_2 = 0.65 \text{ fm}$

was obtained at $E_{\text{Lab}}(^9\text{Be}) = 16$ MeV [MA11], and such discrepancies may be attributed to the limitation of the present one-step DWBA calculations.

The calculation of the inelastic-scattering angular distributions with the incoherent and coherent additions of inelastic scattering cross-sections and amplitudes, respectively, (see Section 2.4.1 for details) are shown in Figs. 4.9 and 4.10. In both cases, the fit to the data underestimates the cross-section at small and large scattering angles. The coherent addition (see Fig 4.10) in particular introduces relatively more and stronger structures which are not seen in the measured cross-section. In addition, the mirrored data points about $\theta_{\text{c.m.}} = 90^\circ$ (open circles) are not entirely consistent with the independent measurements (closed circles) indicating the absence of symmetry. From these observations we, therefore, conclude that symmetry effects are not present in the inelastic scattering channel and that a one-step DWBA calculation sufficiently well describes the data.

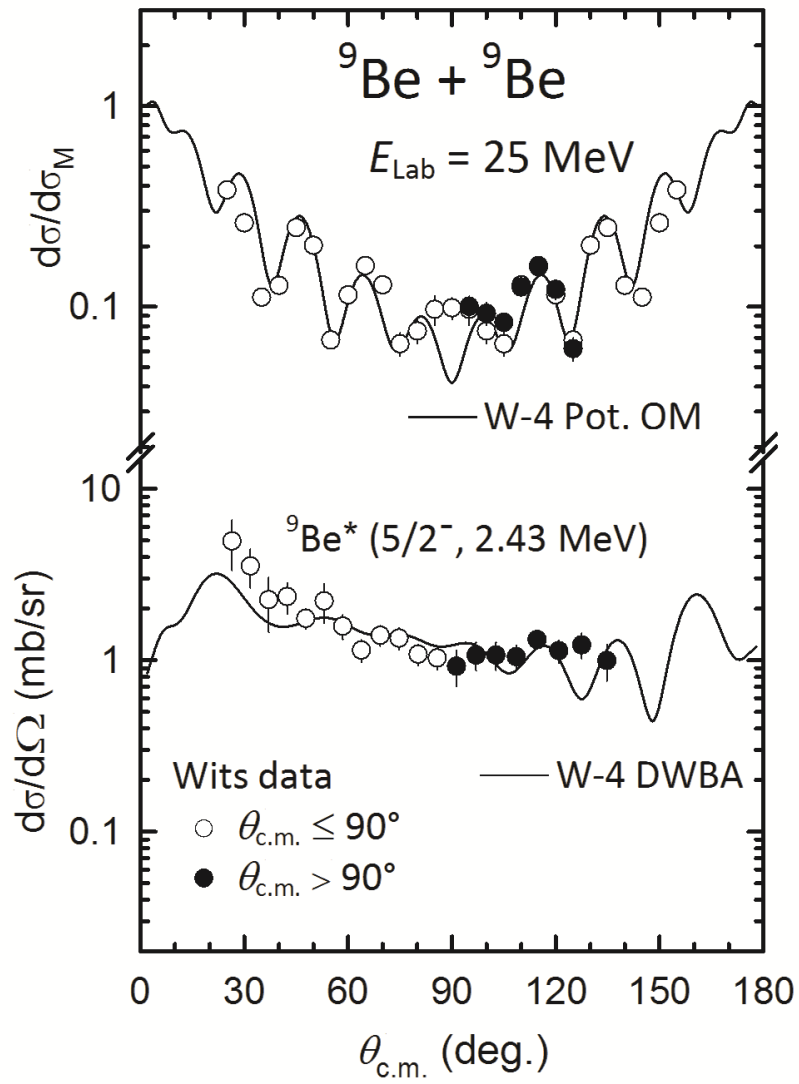


Figure 4.7: Upper part: Angular distributions for the elastic scattering of ${}^9\text{Be} + {}^9\text{Be}$ at $E_{\text{Lab}}({}^9\text{Be}) = 25 \text{ MeV}$. Lower part: Inelastic excitation of the second, unbound, state in ${}^9\text{Be} (5/2^-, 2.43 \text{ MeV})$ at $E_{\text{Lab}}({}^9\text{Be}) = 25 \text{ MeV}$

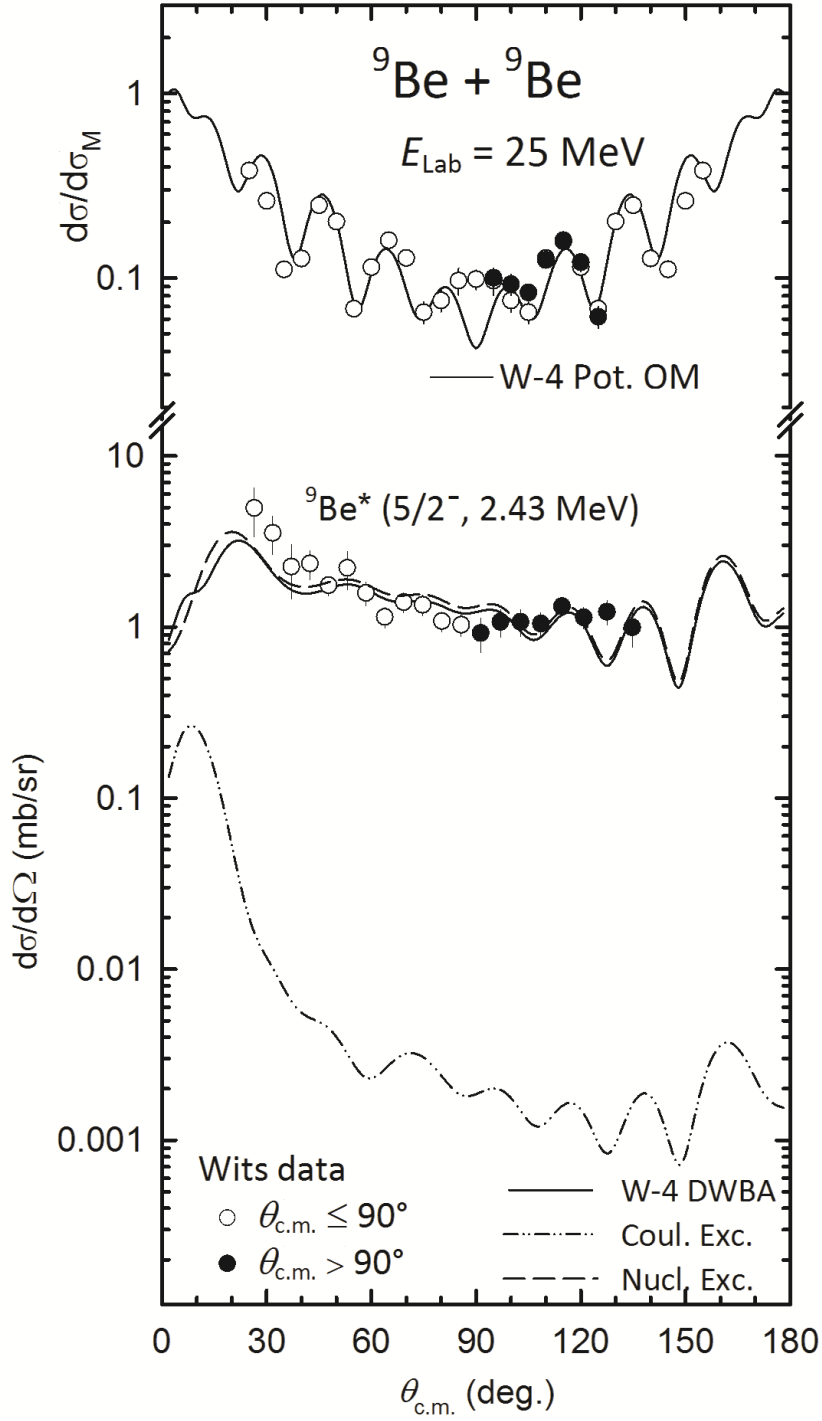


Figure 4.8: *Upper part:* Angular distributions for the elastic scattering of ${}^9\text{Be} + {}^9\text{Be}$ at $E_{\text{Lab}}({}^9\text{Be}) = 25 \text{ MeV}$. *Lower part:* Inelastic excitation of the second, unbound, state in ${}^9\text{Be} (5/2^-, 2.43 \text{ MeV})$ at $E_{\text{Lab}}({}^9\text{Be}) = 25 \text{ MeV}$, showing Coulomb and nuclear excitations.

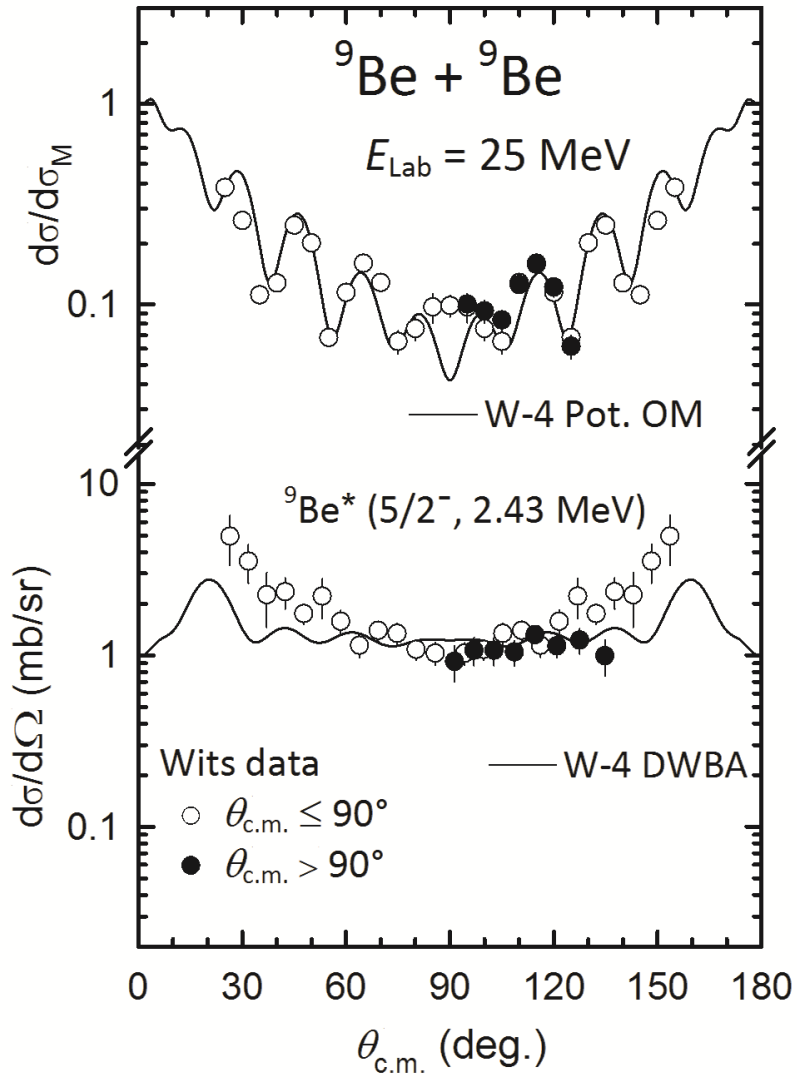


Figure 4.9: *Upper part:* Angular distributions for the elastic scattering of ${}^9\text{Be} + {}^9\text{Be}$ at $E_{\text{Lab}}({}^9\text{Be}) = 25 \text{ MeV}$. *Lower part:* Inelastic excitation of the second, unbound, state in ${}^9\text{Be} (5/2^-, 2.43 \text{ MeV})$ at $E_{\text{Lab}}({}^9\text{Be}) = 25 \text{ MeV}$ using incoherent addition.

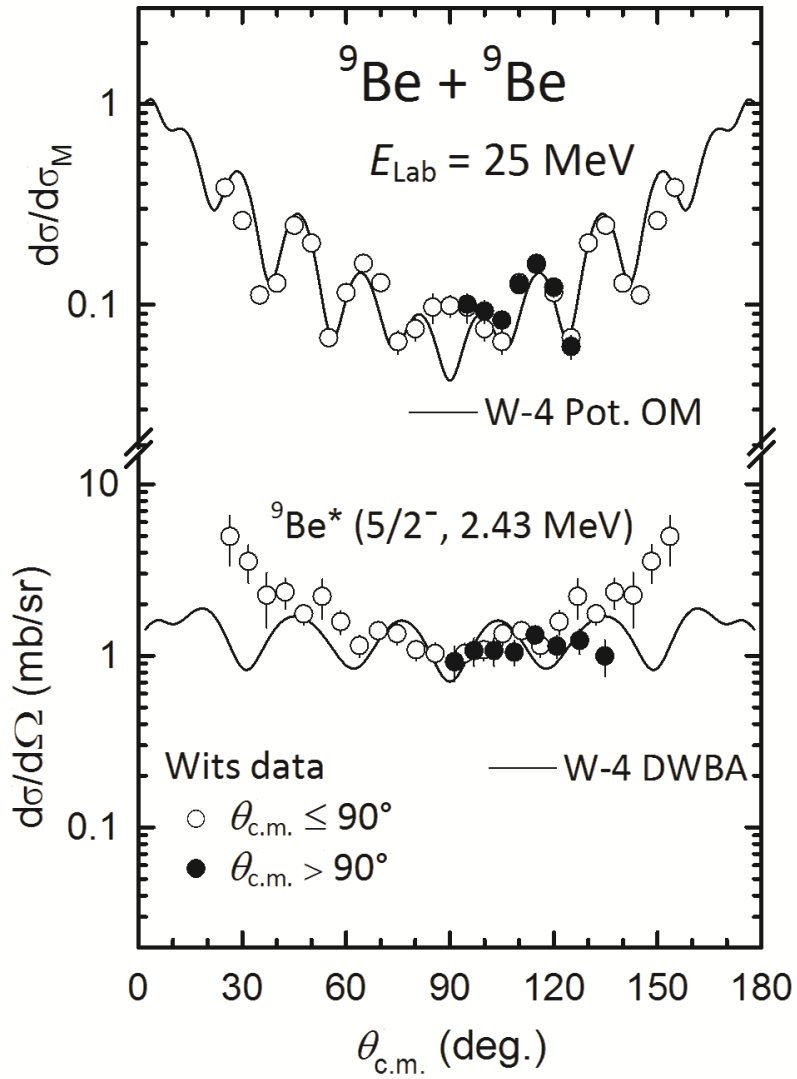


Figure 4.10: *Upper part:* Angular distributions for the elastic scattering of ${}^9\text{Be} + {}^9\text{Be}$ at $E_{\text{Lab}}({}^9\text{Be}) = 25 \text{ MeV}$. *Lower part:* Inelastic excitation of the second, unbound, state in ${}^9\text{Be} (5/2^-, 2.43 \text{ MeV})$ at $E_{\text{Lab}}({}^9\text{Be}) = 25 \text{ MeV}$, using coherent addition.

CHAPTER 5

Conclusions

In this work, elastic and inelastic-scattering angular distributions were measured for the ${}^9\text{Be} + {}^9\text{Be}$ system at $E_{\text{Lab}}({}^9\text{Be}) = 25$ MeV. The elastic scattering angular-distribution was compared with the optical model calculations which provided a good overall fit to the angular distribution. The optical model analysis has shown that at $E_{\text{Lab}}({}^9\text{Be}) = 25$ MeV, the energy-independent optical potential parameters determined by Mayida [MA11] in the energy range $3 \text{ MeV} \leq E_{\text{Lab}}({}^9\text{Be}) \leq 25$ MeV described the elastic scattering angular distribution very well at $E_{\text{Lab}}({}^9\text{Be}) = 25$ MeV. This indicates that these same optical model parameters might also give good fit at other higher beam energies. This can be determined by further measurements.

The one-step DWBA calculation using the optical model parameters leads generally to a better description of the inelastic data. By taking into account only the nuclear excitation in the DWBA, an equally good description of the inelastic angular distribution was obtained. The Coulomb excitation which appears very weak in the DWBA calculation was dominated by the nuclear excitation; this could be attributed to the low proton number of ${}^9\text{Be}$. The incoherent and coherent additions calculated in the DWBA for the inelastic angular distribution were not satisfactory in the angular range $60^\circ \geq \theta_{\text{c.m.}} \geq 130^\circ$. Both were unable to reproduce the experimental cross-sections. The effects of symmetry on the inelastic scattering were investigated by reflecting the measured inelastic scattering data for $\theta_{\text{c.m.}} < 90^\circ$ about $\theta_{\text{c.m.}} = 90^\circ$ and showed that independently measured inelastic scattering cross-sections were not consistent. From these observations it is concluded that symmetry effects in the inelastic scattering channel are not important.

A further study of the inelastic scattering at the highest beam energy for the EN Tandem, i.e. $E_{\text{Lab}}(^9\text{Be}) = 29 \text{ MeV}$ would be desirable or at a higher beam energy. Measurements could be taken at more backward scattering angles to also investigate further the possible structure of the inelastic scattering cross-sections.

References

- [AJ88] F. Ajzenberg-Selove, Nucl. Phys. A490 (1988) 1-225.
- [AU78] E. H. Auerbach, A-THREE: *A general optical model code especially suited to heavy-ion calculations*, Computer Physics Communications 15 (1978) 165-192.
- [BA80] R. Bass, *Nuclear Reactions with Heavy ions* (Springer-Verlag, Berlin 1980) 10-12, 35.
- [BE64] Sergio DeBenedetti, *Nuclear interactions* (John Wiley & Sons Inc., 1964). 74
- [CA78] J. M. Carter, *Inelastic scattering of heavy ions from light nuclei at energies near the coulomb barrier*, Doctor of Philosophy, University of the Witwatersrand, (1978).
- [FE92] R. W. Fearick, WIMPS 2 multi-parameter data acquisition system OS/2, Computer Programme (1992).
- [HO71] P. E. Hodgson, *Nuclear reactions and Nuclear Structure*, (Oxford University Press, 1971).
- [HO78] P. E. Hodgson, *Nuclear heavy-ion reactions*, (Oxford University Press, 1978).
- [JA70] Daphne F. Jackson, *Nuclear Reactions*, (Muthuen & Co Ltd, 1970).
- [JE90] N. A. Jelly, *Fundamentals of nuclear Physics*, (Cambridge University Press, 1990).
- [JI84] Peter Jipsen, Computer programme ELOSS.
- [JI10] M. Jingo, *Characteristics and use of a high resolution ΔE - E gas-ionisation detector for nuclear particle identification*, MSc Research Report, University of the Witwatersrand, (2010).
- [KR88] Kenneth S. Krane, *Introductory Nuclear Physics*, (John Wiley & Sons Inc., 1988).

- [KU10] C. O. Kureba, *Energy Calibration of the 6 MV EN tandem accelerator of iThemba LABS (Gauteng) and measurement of $^{16}\text{O} + ^{16}\text{O}$ elastic scattering*, MSc Research Report, University of the Witwatersrand, (2010).
- [KU60] P. D. Kunz, *Ann. of Phys.* 11 (1960) 275.
- [LA88] F. Lahlou, B. Čujec and B. Dasmahapatra, *Nucl. Phys.* A486 (1988) 189- 206.
- [LE92] W. R. Leo, *Techniques for Nuclear and Particle Physics Experiments, A How-to Approach* (Springer-Verlag Berlin Heidelberg, 1992) 24-25.
- [MA11] I. Mayida, *Elastic and inelastic excitation of an unbound state in the fermionic $^9\text{Be} + ^9\text{Be}$ system near the Coulomb barrier*, MSc research Report, University of the Witwatersrand, (2011).
- [MA68] J. B. Marion and F. C. Young, *Nuclear Reactions Analysis* (North-Holland-Amsterdam, 1968) 39-41, 140-142.
- [MI90] Roy Middleton, *A Negative-Ion Cookbook*, Department of Physics, University of Pennsylvania Philadelphia, PA 19104.
- [OM84] A. R. Omar, J. S. Eck, J. R. Leigh and T. R. Ophel, *Phys. Rev.* C30, (1984) 896-901.
- [SA80] G. R. Satchler, *Introduction to Nuclear Reactions*, (The Macmillan Press Ltd, 1980).
- [TS75] S. F. Tsai and G. F. Bertsch, *Phys. Rev.* C11, (1975) 1634.
- [UN79] E. Ungricht, D. Balzer, M. Hugi, J. Lang and R. Müller, *Nucl. Phys.* A313 (1979) 376-384.
- [YA61] Luke C. L. Yaun and C-S Wu, *Methods of Experimental Physics, Volume 5- Part A* (Academic Press Inc.1961) 4-7.
- [YO77] Richard C. York and R. T. Carpenter, *Nucl. Phys.* A282 (1977) 351-364.

Appendix

Tabulated values of the measured Quantities

Table A1: Elastic scattering measured data of ${}^9\text{Be} + {}^9\text{Be}$ at $E_{\text{Lab}}({}^9\text{Be}) = 25 \text{ MeV}$.

θ_{Lab} (deg.)	$\theta_{\text{c.m.}}$ (deg.)	$d\sigma/d\sigma_{\text{M}}$	Error (\pm)
12.5	25.0	0.3816	0.0054
15.0	30.0	0.2616	0.0043
17.5	35.0	0.1114	0.0059
20.0	40.0	0.1277	0.0061
22.5	45.0	0.2474	0.0068
25.0	50.0	0.2021	0.0184
27.5	55.0	0.0683	0.0053
30.0	60.0	0.1145	0.0057
32.5	65.0	0.1599	0.0108
35.0	70.0	0.1283	0.0087
37.5	75.0	0.0653	0.0087
40.0	80.0	0.0757	0.0099
42.5	85.0	0.0970	0.0162
45.0	90.0	0.0986	0.0119
47.5	95.0	0.1003	0.0110
50.0	100.0	0.0926	0.0119
52.5	105.0	0.0836	0.0080
55.0	110.0	0.1252	0.0105
57.5	115.0	0.1583	0.0082
60.0	120.0	0.1219	0.0135
62.5	125.0	0.0617	0.0081

Table A2: Inelastic scattering measured data of ${}^9\text{Be} + {}^9\text{Be}$ at $E_{\text{Lab}}({}^9\text{Be}) = 25 \text{ MeV}$ for the second, unbound, state ${}^9\text{Be}$ ($5/2^-$, 2.43 MeV).

θ_{Lab} (deg)	$\theta_{\text{c.m.}}$ (deg)	$d\sigma/d\Omega$ (mb/sr)	Error (\pm) (mb/sr)
12.5	26.5	4.9570	1.6177
15.0	31.8	3.5439	0.9036
17.5	37.1	2.2515	0.7982
20.0	42.4	2.3494	0.4835
22.5	47.7	1.7528	0.2361
25.0	53.1	2.2157	0.5776
27.5	58.5	1.5803	0.2556
30.0	63.9	1.1438	0.1680
32.5	69.3	1.3978	0.1895
35.0	74.7	1.3452	0.1889
37.5	80.2	1.0830	0.1492
40.0	85.7	1.0305	0.1546
42.5	91.3	0.9220	0.2170
45.0	97.0	1.0707	0.2019
47.5	102.7	1.0708	0.1995
50.0	108.6	1.0467	0.1739
52.5	114.6	1.3205	0.1416
55.0	120.9	1.1370	0.1688
57.5	127.5	1.2278	0.2081
60.0	134.8	0.9950	0.2400